Received 2 June 2025, accepted 18 June 2025, date of publication 20 June 2025, date of current version 1 July 2025.
Digital Object Identifier 10.1109/ACCESS.2025.3581790

RESEARCH ARTICLE

Optimized Physiological Monitoring System for COVID-19 Using VLC-Based 3D Localization and Markov Chain Analysis

EDUARDO VIERA RIQUELME[1], DIEGO ALONSO CANDIA[2], ISMAEL SOTO[1], (Member, IEEE), CAROLINA LAGOS[3], PABLO PALACIOS JÁTIVA[2], (Member, IEEE), RAÚL CARRASCO[4], CESAR AZURDIA MEZA[5], (Member, IEEE), AND IVÁN SÁNCHEZ[6]
[1]Department of Electrical Engineering, Universidad de Santiago de Chile, Santiago 9170022, Chile
[2]Escuela de Informática y Telecomunicaciones, Universidad Diego Portales, Santiago 8370067, Chile
[3]Facultad de Ingeniería y Negocios, Universidad de Las Américas, Santiago, Providencia 7500975, Chile
[4]Departamento de Contabilidad y Gestión Financiera, Facultad de Administración y Economía, Universidad Tecnológica Metropolitana, Santiago 8320000, Chile
[5]Department of Electrical Engineering, Universidad de Chile, Santiago 8330015, Chile
[6]Department of Networking and Telecommunication Engineering, Universidad de Las Américas, Quito 170125, Ecuador

Corresponding author: Iván Sánchez (ivan.sanchez.salazar@udla.edu.ec)

This work was supported in part by the Project Fondo Nacional de Desarrollo Científico y Tecnológico (FONDECYT) Iniciación under Grant 11240799; in part by the Project FONDECYT Regular under Grant 1211132; in part by STIC-AMSUD under Grant AMSUD220026; in part by Dicyt/Universidad de Santiago de Chile (USACH) under Grant 062413SG; in part by the Escuela de Informática y Telecomunicaciones, Universidad Diego Portales; in part by the Universidad de Las Américas (UDLA) Telecommunications Engineering Degree FICA, UDLA; in part by the Agencia Naciona de Investigación y Desarrollo (ANID) Vinculación Internacional under Grant FOVI240009; in part by the Universidad de Las Américas under Project 563.B.XVI.25; in part by the SENESCYT—Convocatoria Abierta 2014-Primera Fase under Grant Acta CIBAE-023-2014; and in part by the Pontificia Universidad Católica del Ecuador under Project PEP QINV0485-IINV528020300.

ABSTRACT This research presents an optimized physiological monitoring system for COVID-19 patients, integrating Visible Light Communication (VLC)-based three-dimensional localization with Markov Chain Analysis. The proposed system enables real-time tracking of vital physiological indicators while balancing localization accuracy and computational efficiency, making it suitable for real-world healthcare applications. The VLC-based localization system was implemented using three LED beacons and optimized through Particle Swarm Optimization (PSO). The analysis revealed that optimal PSO parameters ($c_1 = 1.9$, $c_2 = 2.1$, and $w = 0.8$) significantly improved positioning accuracy, with 700 to 1100 particles providing the best trade-off between precision and computational cost. Additionally, the system successfully measured and calibrated cough frequency, respiratory rate, and oxygen saturation (SpO_2) using MEMS sensors. The results showed a cough frequency peak at 0.2 Hz, an average respiratory rate of 1.3 breaths per minute, and precise detection of hypoxia events through infrared and red light absorption. To assess disease progression, a Markov Chain Model was developed, analyzing heart rate, temperature, cough frequency, respiratory rate, and SpO_2 levels. The model identified four distinct patient states, ranging from mild to severe conditions, and provided probabilistic insights into symptom deterioration. A heat map analysis confirmed the reliability of state transition probabilities. The study underscores the critical trade-off between localization accuracy and computational efficiency, emphasizing the importance of careful parameter selection for real-time medical applications.

INDEX TERMS COVID-19, physiological monitoring, VLC-based localization, particle swarm optimization, Markov chain analysis, MEMS sensors.

I. INTRODUCTION

The COVID-19 pandemic exposed weaknesses in healthcare systems [1], [2]. Even modern E-Health systems struggle to monitor key physiological parameters. Real-time tracking is crucial for assessing the progression or regression of symptoms. Researchers collaborate to address challenges and improve response capabilities.

A key factor in hospitals is the precise localization of patients and instruments [3], [4], [5]. The tracking of medical

The associate editor coordinating the review of this manuscript and approving it for publication was Barbara Masini.

devices improves care, optimizes resources and increases efficiency [6], [7], [8], [9]. Localization technologies are used in warehouses, offices and transportation systems [10], [11], [12]. Traditional localization technologies, such as GPS [13], fail in the indoors. Signal obstructions from walls, ceilings, and materials cause inaccuracy [7], [10]. WiFi [14], [15], Bluetooth [16], [17], and RFID [18] are alternatives [10]. These methods have high costs, interference, or low accuracy [6], [19], [20]. To overcome these challenges, optical communication systems have been proposed.

Visible Light Communication (VLC) has emerged as a promising alternative. Although VLC lacks omnidirectional coverage and does not penetrate walls, it offers superior positioning accuracy. It also eliminates electromagnetic interference and has low energy consumption [15]. Research on Visible Light Positioning (VLP) has explored different techniques tailored to specific environments. The available resources and spatial constraints influence the VLP methods [21], [22]. Artificial intelligence (AI) improves positioning accuracy and optimizes systems. AI also provides additional functionalities [23].

This study introduces a VLC-based 3D localization system to enhance real-time patient tracking in hospital environments. In addition, biometric sensors continuously monitor patient status. Real-time data are transmitted to a Markov chain model using a VLC channel. The model estimates the recovery or deterioration probabilities [24].

The localization process employs trilateration to estimate 3D coordinates (X, Y, Z). Calculate distances from LEDs using received power measurements. This approach minimizes the errors between the measured and predicted power. The VLC channel model improves positioning accuracy.

The problem's non-linear nature requires an optimization strategy. PSO is used to explore search spaces efficiently. It helps in finding optimal solutions for localization problems. Each particle represents a possible receiver position. Particles refine positions using individual and neighboring experiences. This process minimizes the localization error [18]. Fig. 1 shows the methods used in VLP systems. It highlights common techniques in existing research.

After this introduction, the structure of this article is organized as follows: Section II presents the related work in general. Section III discusses related work on indoor positioning systems. Section IV details the VLP methodology and the evolution of COVID-19. Section V presents the results and discussion. Finally, Section VII summarizes the key findings, highlights the contributions of this research, and suggests potential areas for future work.

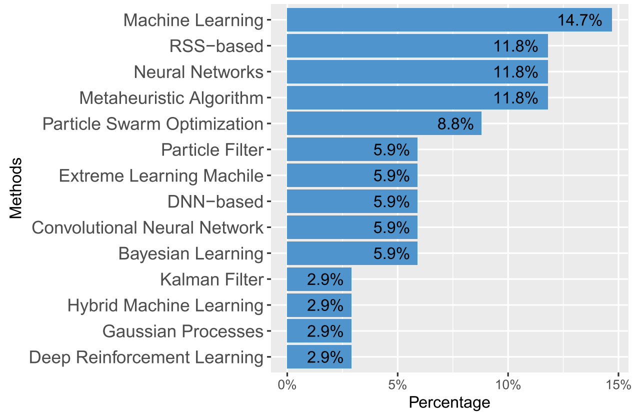

FIGURE 1. Distribution of methods used in VLP systems.

II. RELATED WORK

A. FIRST PHASE: RSS-BASED SYSTEMS AND OPTIMIZATION TECHNIQUES

A renowned metric widely used by VLC positioning systems is Received Signal Strength (RSS). This metric is useful for estimating the position of objects. Some works combine this measurement with AI to improve localization accuracy in indoor environments. For example, [13] propose a system based on VLC and inertial navigation using particle filters to determine the position of a target. However, these types of system faced significant limitations in terms of accuracy mainly due to interference conditions or when Line-Of-Sight (LOS) is unclear.

To handle some of these limitations, several studies propose optimization algorithms. In [20] the PSO algorithm is presented to improve positioning. This approach represents a significant advancement, but the need for greater accuracy and adaptability to dynamic environments quickly became evident.

B. SECOND PHASE: INCORPORATION OF ARTIFICIAL INTELLIGENCE

As the limitations of RSS-based systems became apparent, the integration of AI techniques began to transform VLC-based indoor positioning systems. A milestone in this transition was the work of [14], which applied machine learning to improve signal processing in VLC systems, allowing improvements in both accuracy and efficiency. This study showed that machine learning techniques could address issues like signal interference and variability in indoor lighting conditions, factors that had negatively impacted traditional RSS-based approaches.

The incorporation of neural networks into VLP systems is a key advance. For example, the use of neural networks improves localization accuracy in a VLC-based positioning system [25].

C. THIRD PHASE: RECENT ADVANCES AND NEW APPLICATIONS

In recent years, VLC research has shifted toward combining deep learning algorithms with advanced optimization techniques. An example is the work of [26], which used a combination of Extreme Learning Machine and metaheuristic algorithms to improve positioning accuracy in VLC systems. This approach has proven highly effective in improving performance under complex conditions, such as in Non-Line-of-Sight (non-LOS) environments.

Furthermore, recent studies, such as [27], have investigated how the use of deep neural networks and input parameter optimization techniques can mitigate errors in non-LOS environments, representing a significant advancement in applying VLC systems in spaces where light signals may be obstructed.

Another key advancement has been the use of deep reinforcement learning in positioning systems in dynamic environments. These studies have demonstrated that deep reinforcement learning can enhance VLC systems' ability to adapt to changing conditions, making them ideal for use in industrial and commercial environments [28].

D. FOURTH PHASE: NEW FRONTIERS IN VLC AND AI

Recent research is exploring the potential of VLC in highly dynamic environments, such as smart factories and autonomous vehicles. For example, [29] investigated the use of VLC for positioning in high-speed rail systems, demonstrating how the combination of VLC and AI can improve accuracy in mobile environments.

Another emerging approach is the use of hybrid deep learning algorithms, who demonstrated that combining deep learning algorithms with light modulation techniques can significantly improve indoor positioning accuracy [30].

The study by [23], on the other hand, provides a comprehensive review of AI methodological approaches in VLC positioning for Internet of Things (IoT) applications. This work highlights how the convergence of AI and VLC technology can enable more sophisticated applications, such as real-time asset tracking and resource management in smart factories.

E. FUTURE PERSPECTIVES AND CHALLENGES

Over the past few years, VLP has significantly advanced thanks to the integration of techniques such as deep learning, non-linear optimization, and the use of Kalman filters [31], [32]. Early studies focused on leveraging the optical properties of light, such as depolarization and reflection, to improve accuracy in indoor environments [33]. However, more recent research has incorporated advanced hybrid models and algorithms to address the limitations of traditional methods [34]. The introduction of 5G/6G networks and artificial intelligence into these systems has enabled improved adaptability and precision, especially in dynamic environments [35], [36]. This demonstrates that the evolution of VLP is moving towards more advanced and precise applications, expanding its reach across various industries and complex scenarios. The evolution of indoor positioning systems based on VLC has gone through several phases, driven by advancements in signal processing technologies and, more recently, by the incorporation of AI and machine learning algorithms. This discussion reviews key developments in this field, using a wide range of recent studies to demonstrate how these systems have improved in accuracy, efficiency, and applicability in complex environments. Looking ahead, it is clear that the convergence of VLC and AI will continue to be a key area of research. Recent studies, such as [37], which propose the use of optimized machine learning models for VLC-based positioning systems in wireless sensor networks, represent a trend towards optimizing systems in low energy consumption environments.

Finally, the work by [38], which combines synthetic data and deep neural networks to mitigate signal issues at tilted angles in VLC systems, opens up new possibilities for the use of these systems in industrial and autonomous navigation applications.

- Develop and implement a VLP system that leverages existing LEDs emitting at different wavelengths. This method enables localization without continuous data transmission, simplifying the system infrastructure and decreasing operational costs.
- Analyze the adjustment of the PSO algorithm in 3D localization, studying the impact of the main parameters of the technique on positioning error, such as cognitive factor, social factor, and inertial weight.
- Perform a comprehensive analysis of the impact of PSO parameters—such as the number of particles and iterations—on system performance, offering insights to balance accuracy and computational efficiency. To enhance accuracy, we integrate the PSO algorithm, enabling precise three-dimensional localization. This approach ensures reliable and accurate positioning without the requirement for constant communication between the transmitters and receivers [20]. Moreover, it is common to treat localization as an optimization problem that can be effectively addressed using meta-heuristic algorithms to improve accuracy [18].
- Develop a HRV monitoring sensor based on ECG enables the detection of intervals between "R" peaks in the QRS complex of an electrocardiogram, providing valuable information about heart rate variability (HRV). This variability reflects the activity of the autonomic nervous system, allowing for the assessment of both sympathetic and vagal functions. Monitoring HRV is essential in clinical settings where autonomic dysfunction is suspected. Key metrics include the average R-R interval, SDNN (standard deviation of R-R intervals), NN50, pNN50, and rMSSD, each contributing specific insights into the patient's cardiac health.
- Present the estimation and correlation of physiological variables such as (blood oxygen saturation, HRV, cough counter, respiratory frecuency and body temperature) to predict the progression of respiratory infections such as COVID-19 based on Markov Chains.

III. RELATED WORK ON INDOOR POSITIONING AND PHYSIOLOGICAL MONITORING SYSTEMS

This section presents a specific literature review on related work in indoor positioning systems and Physiological Monitoring technologies.

A. RELATED WORK ON INDOOR POSITIONING

In this regard, multiple wireless technologies have been proposed for indoor positioning purposes. Alternatives such as WiFi [14], [15], Bluetooth [16], [17], and RFID [18], among others [10], have emerged as enabling technologies for this application. However, these technologies can be costly, complex to implement, cause electromagnetic interference with other equipment, or present significant inaccuracies [6], [19], [20]. To address these challenges, optical communication systems have been proposed, and VLCs have emerged as a promising solution. A comparison of some of these technologies is shown in [15], with the results presented in Table 1.

This comparison highlights that, although VLC does not penetrate walls and is not omnidirectional, it offers superior precision compared to the wireless technologies mentioned. Additionally, VLC does not cause electromagnetic interference and has low energy consumption. Furthermore, existing LED infrastructure can be leveraged to enable indoor positioning. For these reasons, VLC emerges as a viable option for the localization of indoor targets.

The implementation of VLC to enable target positioning in indoor environments represents an innovative solution that is rapidly gaining traction. Several studies on VLP have explored different techniques based on the specific environment, available resources, human requirements, required dimensions, and other factors [11], [12], [23]. Moreover, the application of AI in indoor locations has emerged as a promising tool for enhancing accuracy, optimizing proposed systems, and providing additional functionalities [15].

Additionally, indoor localization can be addressed as an optimization problem where metaheuristic algorithms are useful tools [18]. PSO is one of these techniques that help to solve the optimization problem, which is widely used in problems with continuous solutions spaces [20].

The dependence on continuous data transmission between a transmitter and a receiver to locate a target, is a characteristic of traditional VLP systems. However, there are environments where uninterrupted data transmission and reception face various challenges [16], [17]. Therefore, data flow, system performance and robustness are affected by factors such as signal blockage, multipath interference, and other environmental changes. Moreover, most active VLP systems require complex signal processing infrastructure to modulate and demodulate data. This requirement adds costs and complexity to the system [13], [19]. To address these issues, this work proposes a three-dimensional localization system.

The system proposed consists of three LEDs with different wavelengths as transmitters and leverages these differences to distinguish signals to eliminate the need for continuous data transmission. Then, the system calculates the target position based on RSS metric. Having this measurement, distance between each transmitter and receiver can be determined. Moreover, the approach proposes the localization problem as an optimization problem. Therefore, the PSO algorithm is used to solve the optimization equation, and then enabling precise three-dimensional localization.

The field of VLP has seen considerable advancement through the integration of AI and metaheuristic optimization techniques. AI methods, such as machine learning algorithms, have significantly enhanced the accuracy and adaptability of VLP systems [12], [15]. Supervised learning approaches, including neural networks and support vector machines, have been used to predict indoor positions based on received signal patterns, improving the system's ability to handle dynamic environments [15]. Furthermore, unsupervised learning methods, such as clustering and dimensionality reduction, have facilitated the analysis of large datasets to improve localization precision without extensive manual calibration [11].

In this sense, the authors of [13] employ a particle filter to enhance the accuracy of the positioning method when the target is in motion. Meanwhile, the work in [20] presents an indoor localization system based on an extended Kalman filter, which combines the receiver's estimated position using VLP with inertial navigation data. This combination is designed to tackle challenges such as direct LOS obstruction and the effects of multipath reflection.

Metaheuristic algorithms, such as Genetic Algorithms (GA) and PSO, among others, have also played a crucial role in optimizing VLP systems. These algorithms are particularly effective for solving complex, non-linear optimization problems inherent in VLP. For example, GA has been used to optimize the placement and configuration of LEDs and photodiodes to minimize localization errors, which has been shown to be robust in various indoor scenarios [15]. Similarly, PSO has been applied to improve positioning accuracy by optimizing the models used in VLP, demonstrating high efficiency and convergence speed in dynamic environments [11], [19], [20]. However, despite the known use of PSO in VLP, there are no articles that address the parameters of the PSO algorithm and how they affect the accuracy of the systems.

On the other hand, regarding passive VLP, several works propose localization based on VLC without data transmission. For instance, the paper in [16] presents a new methodology for indoor localization using visible light emissions, which does not require users to actively participate in the process. Their approach utilizes a network of luminaires and receivers on the ceiling, measuring the impulse responses between each source-receiver pair to locate objects within a room.

In [17] it reports a VLP system that achieves target localization utilizing PD embedded in a wall to capture the RSS of ambient light. In this work the system does not require active devices or tags carried by the target for localization, nor does it require modifications to the lighting infrastructure. Instead, this approach takes advantage of variations in the ambient light. The light fluctuations caused by movements of

TABLE 1. Comparison of localization techniques.

Technique	Transmission Range	Omnidirectional	Interference With	Penetrates Walls	Energy Consumption	Accuracy Range
RFID	Long	Yes	RF signals	Yes	Low	cm
Acoustic	Short	Yes	Acoustic	Yes	Medium	cm
Bluetooth	Short	Yes	RF signals	Yes	Low	cm
WiFi	Long	Yes	RF signals	Yes	Medium	cm
UWB	Short	Yes	Immune to interference	Yes	Medium	cm
VLC	Long	No	Light	No	Low	mm

objects allow localization by analyzing variations in the light source.

Finally, the research in [15] explores passive VLC localization utilizing the reflective properties of objects and LED luminaires. This study presents geometric models, a testbed implementation, and empirical evaluations, demonstrating the feasibility of achieving accurate localization without the need for objects to carry any optical receiver. The proposed method can track the object with high accuracy and identify the object's ID passively.

There are still challenges in passive VLP systems, even with these advancements. For example, adding additional infrastructure is still necessary to reduce precision errors. Also, the active participation of the targets is a widely adopted standard.

B. RELATED WORK ON PHYSIOLOGICAL MONITORING SYSTEMS

For this research, it is possible to determine well-defined topics that are related to Physiological Monitoring systems according [39], which are defined by the monitoring of physiological parameters and their respective systems for data transmission such according to [40].

Another point of interest is the application of different algorithms that allow the correct discrimination or data classification, as well as the stochastic establishment of the behavior of the physiological and/or hemodynamic parameters that allow to show how the disease is developed with a certain degree of certainty. This tool will enable to establish priorities in the medical attention of patients, for example, as with the results obtained by using smartwatch data [41]; and at a macro level, it can be applied to monitoring a population [42].

In search of better and more effective tools to handle this pandemic, multidisciplinary research groups have established developments related to Physiological Monitoring systems that focus mainly on remote assisted systems [43], [44], [45]. This research defines an architecture of Physiological Monitoring systems based on minimal MEMS sensors, for the later establishment of complex data structures that are represented by visualization systems through smartphones and/or dashboards.

According to [40], the systems mentioned above should be incorporated into data processing systems, specifically based on processing and/or prediction algorithms to obtain the progression of the disease through the comparison of permissible levels, as well as the stochastic study of the progress of the disease in the population. On the other hand, the statistical data allow one to find known patterns that can generate a classification regarding an affected population, as researched in [46] and [47]. In this sense, the previously cited references set the background for the development of the present study. In parallel, a detailed knowledge of symptoms and levels of physiological parameters requires the establishment of parameters that can quickly set the necessary alarms for the correct treatment of people affected by COVID-19. In this case, the basis for the development and application of the process will be the Markov chain [48], [49]. In addition, other hemodynamic parameters are incorporated to set certain characteristics of people affected by COVID-19, such as HRV [50], [51], [52]. With the previous background, this research aims to use a low-cost system for the acquisition of physiological data using Physiological Monitoring systems, wherein the information to be collected points to an estimation of the central body temperature, HRV, respiratory frequency, cough counter and a sensor for the body position. The data collected will be used as input to establish the status of the disease progression, which will be processed through Markov chains. The result will provide the probability of a change in the state of a person, whether to a worse disease stage or an improvement in the health status of the patient [53]. Thus, an improvement in predictive diagnosis can be obtained with respect to the treatments that COVID-19 patients should receive based on disease progression.

IV. MATERIALS AND METHODS

Fig. 2 illustrates a simplified diagram of the proposed system, organized into four layers. Each transducer includes photodetectors, LEDs, a power control button, and standard connectors. These transducers operate in pairs, with one unit placed at the base of the bed and others located on the floor, walls, bed headboards, ceiling, patients, or attached to medical equipment. All VLC units—whether mounted on the ceiling or on the patient—are designed as transducer capable of both transmitting and receiving data, enabling a bidirectional VLC link for localization and physiological sensor data transmission. During the third stage, PSO algorithms will be implemented to improve the precision of the location of the patient and equipment, adhering to the methodology outlined in Section IV-C1. Furthermore, Markov chains will produce states using physiological data, as outlined in Section IV-C2.

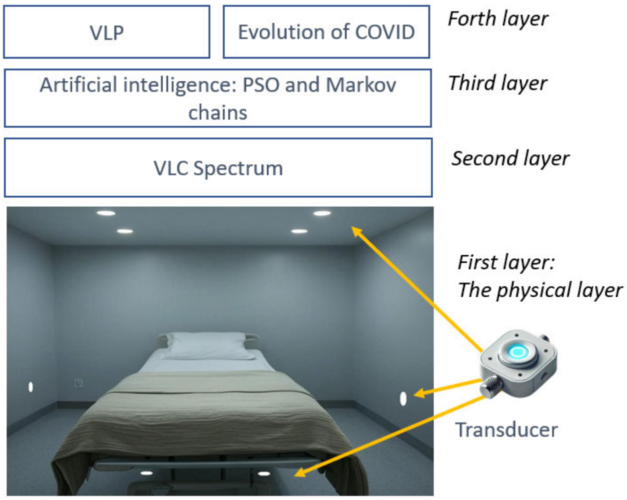

FIGURE 2. **Simplified diagram of the proposed system.**

For example, suppose that a transducer is placed on the patient's chest and four transducer are installed on the ceiling of layer 1. Among these four transducer, the three strongest signals are selected and the data are transmitted through the VLC channel of the second layer. Then, using the third layer with PSO and the VLP technology of the fourth layer, a position reference (x_0, y_0, z_0) is calculated. This initial position, which offers higher accuracy compared to other methods, as explained in III, is used as a reference to calculate the respiratory frequency, assuming variations along the z-axis, which is also the most stable signal according to the description in Section IV-C2f. In a similar manner, a transducer positioned at the throat conveys the respiratory sequence to the Markov chain methodology employed in the third layer, as well as to the COVID-19 evaluation module. This scenario exemplifies a plausible application of the localization system.

If the transducer processors at the physical layer have sufficient processing capacity, the VLC layer can be shifted to the fourth layer. In this scenario, digital processing with artificial intelligence and VLP-based positioning will be performed locally, utilizing the algorithms from Section IV-C1, while Markov chains will continue to generate states using physiological data based on the algorithms in Section IV-C2, and they will be consolidated on a central server.

A. FIRST LAYER: THE PHYSICAL LAYER

The first layer represents the physical layer, comprising beds, biometric sensors, and transducer that facilitate uplink and downlink communication for the next layer. Additionally, curtains play a dual role by isolating patients and enhancing optical communication, which can be purely light-based or a hybrid with radio frequency. It is important to note that the beds are not designed for movement; they have wheels primarily for cleaning purposes, as patient transportation is carried out using separate stretchers.

B. SECOND LAYER: VLC

Depicts the communication spectrum based on VLC as well as its hybrid version with radio frequency. However, this study focuses exclusively on the optical channel.

1) VLC SYSTEM MODEL

This section presents the VLC model that enables the localization system to determine the position of a target within a given environment. We describe the transmitters, receiver configuration, and mathematical representation of the VLC channel. The proposed localization system builds on previous research, expanding the capabilities and application of the approach presented in [6].

2) TRANSMITTER SETUP

To take advantage of the existing lighting infrastructure, we propose the use of three optical transmitters, each consisting of a single LED. These LEDs emit white light at distinct wavelengths, carefully selected to be distinguishable by the receiver while remaining imperceptible to humans. This design allows the system to identify the source of the signals without requiring additional identification data transmission, allowing for continuous light emission at a constant power level.

To accurately apply trilateration techniques, it is essential to know the precise positions of the transmitters within the environment. Let each LED i, where $i = \{1, 2, 3\}$, be located at coordinates (x_i, y_i, z_i) in a 3D space, representing their fixed positions within the room. Fig. 2 illustrates the general scheme of the localization system, showing the positioning of the LEDs and the receiver's PDs. For practical purposes, we assume that all three LEDs are vertically aligned and oriented towards the floor, providing a direct LOS to the receiver.

3) RECEIVER CONFIGURATION

The receiver is designed to differentiate the incoming light beams from the various transmitters. It consists of three PDs, each equipped with an optical filter corresponding to the wavelengths used by the LEDs. This setup is illustrated in Fig. 2. Let (x_j, y_j, z_j) with $j = \{1, 2, 3\}$ represent the position of PD j within the receiver. For practical purposes, we assume that all three PDs are located at the same point due to their small separation. This simplification allows us to treat the receiver as if all PDs share the same position. Consequently, the distance between LED i and the receiver, originally denoted as d_{ij}, is simplified to d_i. This approach is applied to other relevant parameters, such as incidence angles and gains, which are also simplified to a single representative value per LED to facilitate the modeling process. Another consequence of assuming that each PD uses the same position, is that the incidence angle (ψ_{ij}) of the light beams from LED i on PD j is the same for each PD simplifying to ψ_i.

The relevant angles are ϕ_i, the angle from the LED i to the receiver, and ψ_i, the incidence angle of the light beam in the PD. Given the alignment of the PDs pointing vertically upward and the LEDs downward, we infer that $\phi_i = \psi_i$.

Also, it is important to consider the gain of the optical concentrator for each PD. The following expression presents this parameter [54]:

$$g_j(\psi_i) = \begin{cases} \dfrac{n_j^2}{\sin^2 \Psi_j}, & 0 \leq \psi_i \leq \Psi_j \\ 0, & \psi_i > \Psi_j, \end{cases} \tag{1}$$

where n_j denotes the refractive index of the optical concentrator, and $\Psi_j < \pi/2$ represents the Field of View (FoV) of the PD j. Furthermore, the optical filter gain $T_j(\psi_i)$ also impact on signal reception, influencing directly on the amount of light detected by the PD j. Neglecting this factor could lead to inaccurate estimations of the received power, which in turn would degrade the accuracy of the localization system.

The proposed system considerers a static receiver, because it is designed for scenarios where the objectives are in a fixed position, such as hospital beds or stationary monitoring points. With this assumption, the localization model is simplified and the system increases the accuracy in localization due to the minimization of uncertainties related to user movement.

4) INDOOR VLC CHANNEL MODEL

Although this work does not directly use the Color Shift Keying (CSK) modulation mechanism for data communication, it employs a similar approach by leveraging the properties of light and its propagation. Specifically, the methodology utilizes the received power to localize the target, taking into account various factors that affect the VLC channel.

Assuming no interference between the LEDs, the PD j accepts only the signal from LED i via the LOS channel. This assumption is valid because each LED emits at a different wavelength, allowing the receiver to distinguish between the signals. Thus, the equation for P_{LOSij} is [55]:

$$P_{LOSij} = H_{LOSij}(0)P_{ti} + P_{Noise}, \tag{2}$$

where P_{LOSij} represents the received power by PD j from LED i, P_{ti} is the transmitter power of LED i, and P_{Noise} represents the noise power. The channel gain H_{LOSij} can be described mathematically as [54]:

$$H_{LOSij}(0) = \begin{cases} \dfrac{A_j(m_i+1)}{2\pi d_i^2} \cos^{m_i}(\phi_i)\cos(\psi_i)T_j(\psi_i)g_j(\psi_i), \\ \qquad 0 \leq \psi_i \leq \Psi_j \\ 0, \qquad \psi_i > \Psi_j, \end{cases} \tag{3}$$

where A_j denotes the area over which the PD j receives light and m_i represents the Lambertian order.

Given that $\psi_i = \phi_i$, we derive:

$$P_{LOSij} = \frac{A_j(m_i+1)}{2\pi d_i^2} \cos^{m_i+1}(\phi_i)T_j(\psi_i)g_j(\psi_i)P_{ti}. \tag{4}$$

Moreover, the noises considered in this study are the thermal and shot noises, as these are the predominant sources of noise in photodetectors used in optical communication systems, affecting the accuracy of signal reception [56], [57].

Additionally, this study employs a channel model based on the assumption of LOS, which is a common practice in VLC-based localization studies [58], [59], [60]. While real-world scenarios may introduce obstructions, this approach simplifies system implementation and provides a solid foundation for evaluating its feasibility under ideal conditions, in line with previous studies in the literature.

5) MODEL OF A CHANNEL BASED ON CSK/QAM MAPPING

Three different colors are used for positioning due to their simplicity and low cost. Furthermore, the process of translating an M-CSK constellation into an M-QAM constellation is proposed. The original color space, created by the 1931 Commission Internationale de l'Éclairage (CIE) and based on experimental findings of human color perception, is depicted in the upper left corner of Fig. 3. A color space is a multidimensional collection that contains all the possible hues a specific color model can produce. On the right side of Fig. 3, the linked points are displayed as clusters, with a total of 2^{2^i} points for each $i = 0, 1, 2, 3, \ldots$. Fig. 3 illustrates the mapping process used to systematically convert the points in the M-CSK constellation into the M-QAM constellation. The resulting clusters reveal the constellation structure, facilitating the visualization of the mapping relationship across various values of i [61].

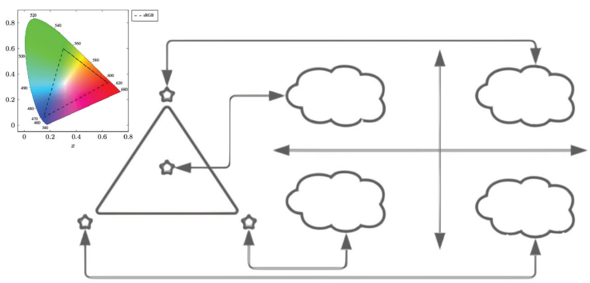

FIGURE 3. General CSK/QAM assignment.

6) EUCLIDEAN DISTANCE CALCULATION

The objective is to obtain the distance between the LED i and the target. Knowing the position of each LED, let (x_t, y_t, z_t) be the unknown location of the target. The Euclidean distance from the LED i to the receiver can be expressed as:

$$d_i = \sqrt{(x_i - x_t)^2 + (y_i - y_t)^2 + (z_i - z_t)^2} \tag{5}$$

Considering the right triangle formed by the distance from the height of the receiver to the position of the LEDs on the ceiling, the relationship can be expressed as:

$$\cos(\phi_i) = \frac{z_i - z_t}{d_i} \tag{6}$$

By combining equations (4) and (6), we obtain:

$$P_{LOSij} = \frac{A_j(m_i+1)}{2\pi} T_j(\psi_i) g_j(\psi_i) P_{ti} \frac{(z_i - z_t)^{m_i+1}}{d_i^{m_i+3}} \tag{7}$$

Rearranging equation (7), we derive:

$$d_i = \left(\frac{A_j(m_i+1)}{2\pi} T_j(\psi_i) g_j(\psi_i) P_{ti} \frac{(z_i - z_t)^{m_i+1}}{P_{LOSij}} \right)^{\frac{1}{m_i+3}} \tag{8}$$

It is observed that the equation depends solely on the received power at PD j.

C. THIRD LAYER: ARTIFICIAL INTELLIGENCE: PSO AND MARKOV CHAINS

Represents the artificial intelligence methods used, such as *Particle Swarm Optimization* (PSO) and Markov chain models.

1) PARTICLE SWARM OPTIMIZATION METHODOLOGY

After acquiring the distance estimates between the receiver and each of the LEDs, the task of finding the target can become an optimization problem. Given that the positioning process occurs in a continuous space, the PSO algorithm is a suitable choice due to its ability to handle problems with a wide range of possible solutions.

PSO is a metaheuristic inspired by the social behavior of swarms, such as flocks of birds, insects, fish, and other creatures, where the movement of each individual is influenced by a combination of personal decisions and group behavior. Similarly, in the PSO algorithm, a group of particles is initially spread across the space and moves based on the results of an objective function obtained by both the individual and the group.

The algorithm 1 shows the pseudocode of the PSO technique. Initially, particles are initialized by defining a position within the space, a velocity indicating the amount of movement in the next iteration, and *pbest* and *gbest*, which represent the best objective function value obtained individually and socially (i.e., a variable common to the entire swarm), respectively. The positions where these results were achieved are also stored. The $pbest_p$ is known as the cognitive factor of the particle p, representing the individual's ability to improve based on their results. In contrast, *gbest* is known as the social factor, indicating how much the success of the group influences the particle.

In each iteration, the same steps are performed for all particles. First, the velocity of the individual is updated according to the expression:

$$v_{t+1} = wv_t + r_1 c_1 * (pbest_p - POS_p) + r_2 c_2 (gbest - POS_p), \tag{9}$$

where w is the inertia weight, r_1 and r_2 are uniformly distributed random numbers in the range $[0, 1]$. POS_p is

Algorithm 1 Particle Swarm Optimization Algorithm

```
Particle initialization by dividing the XY plane
for iteration do
    for all particle do
        Update velocity
        Update position
        Evaluate the objective function value of the particle
        if Particle objective function value < pbest then
            Update pbest
        end if
        if Particle objective function value < gbest then
            Update gbest
        end if
    end for
end for
```

the position of the particle, and c_1 and c_2 are acceleration coefficients that determine the influence of the cognitive and social factors, respectively.

Next, the algorithm updates the position of particle p for the next iteration based on:

$$POS_{t+1} = POS_t + v_{t+1}. \tag{10}$$

2) MARKOV CHAINS

Part of the system was modelled to establish the probability of progress or regression in the symptomatology of COVID-19 patients.

Considering that the system discreetly evolves as ($k = 0, 1, \ldots, n$), which is in a state i_k; thus, at the moment $k-1$ it is in the state i_{k-1}. Formally:

$$\begin{aligned} P(X_k = i_k \mid X_0 = i_0, \ldots, X_{k-1} = i_{k-1}) \\ = P(X_k = i_k \mid X_k = i_{k-1}) \\ = p_{i_{k-1}}, i_k. \end{aligned} \tag{11}$$

Markov chains can be described by using matrixes as follows. If $p_k(k), \ldots, p_n(k)$ corresponds to the probabilities of n states at time k, $p_{ij}(k)$ is the probability of evolution or change from the state i to j at time k, for $k = 1 \leq i, j \leq n$. That is:

$$\begin{aligned} p_1(k-1) &= p_{11}(k)p_1(k) + \ldots + p_{1n}(k)p_n(k) \\ &\vdots \\ p_n(k-1) &= p_{n1}(k)p_1(k) + \ldots + p_{nn}(k)p_n(k), \end{aligned} \tag{12}$$

which is represented by using matrixes as:

$$\begin{pmatrix} p_1(k+1) \\ \vdots \\ p_n(k+1) \end{pmatrix} = \begin{pmatrix} p_{11}(k) & \ldots & p_{1n}(k) \\ \vdots & \ddots & \vdots \\ p_{n1}(k) & \ldots & p_{nn}(k) \end{pmatrix} \begin{pmatrix} p_1(k) \\ \vdots \\ p_n(k) \end{pmatrix}. \tag{13}$$

Due to the characteristics of this study, homogeneous Markov chains are selected, whose structure is composed of a matrix called ''state matrix'', which will hold the information corresponding to all of the parameters to be used at this stage, wherein the following vector can be defined:

$$A_{in} = \begin{pmatrix} HRV(k) & Co(k) & SpO2(k) & Tc(k) & Fr(k) \end{pmatrix}. \tag{14}$$

This matrix A_{in} contains the input values which will allow to establish the states of the state matrix, which is described as:

$$A_{in} = \begin{pmatrix} p_{11}(k) & \dots & p_{11}(k) \\ \vdots & \ddots & \vdots \\ p_{n1}(k) & \dots & p_{nn}(k) \end{pmatrix}. \quad (15)$$

Then, it can be mentioned that a Markov chain is homogeneous if none of the terms of $p_{ij}(k)$ depend on k, which is adjusted to this study since the states, being an intersection of conditions that generate them, not in a time-space but in a space of probabilities of occurrence of a determined condition pattern, make this pattern in fact "not dependent of t". Therefore, the following must be accomplished:

$$p(k) = A^k p(o), \quad (16)$$

which means that the probability at the instant k will be equal to the state transition matrix raised to the kth power times an initial state $p(0) = (p_1(0), \dots, p_n(0))$.

With these definitions, now it is necessary to establish the steady state of the chain, therefore, through the stationary distribution, it is possible to establish the distribution of a steady state for the states of a chain that is independent from the initial distribution:

$$\pi = \lim_{k\to\infty} p(k), \quad (17)$$

which, applied to a homogeneous chain is expressed as:

$$\pi = \lim_{k\to\infty} p(k) = \pi = \lim_{k\to\infty} A^k p(0) = (\lim_{k\to\infty} A^k)p(0). \quad (18)$$

a: STATE MATRIX

As mentioned before, this matrix was built under the concept of "information" that complies with a "condition" to produce a "state". These events were considered as fully probabilistic and time-independent. Given that COVID-19 infection is a disease that progresses by "stages" or states, it is possible to model this matrix as a function of the information obtained from the parameters previously shown.

The following parameters were used to create the matrix:

- GRV_1 is the variability of heart rate.
- TCC_1 is the core body temperature.
- CT_1 is the cough frequency.
- CR_1 is the respiratory frequency.
- $SpO2_1$ is the oxygen saturation in blood.

By using the above parameters, the state matrix is defined as follows in equation (19):

$$A_{in} = \begin{pmatrix} HRV_1 & TCC_1 & CT_1 & CR_1 & SpO2_1 \\ \vdots & \vdots & \vdots & \vdots & \\ HRV_n & TCC_n & CT_n & CR_n & SpO2_n \end{pmatrix}. \quad (19)$$

However, since the information to be stored in the state matrix A_{in} is continuous information that needs to be encoded in order to study the phenomenon in a discreet form, thus, five levels of disease progress were established. These levels were prepared in such a way that the disease progression is linear. Said progression must emulate a development time k wherein each of the iteration comparisons is performed, *i.e.* each period k is a function of the n iterations of the information stored by the vector A_{in}.

Therefore, codification of the states was processed by rules that allow weighting in order to distinguish the different states, and this weighting was a function of value T_p. The value ranges per each state are shown in Table 2.

TABLE 2. Rules of formation of the state matrix.

	HRV (BPM)	Temp. ($°C$)	Cough counter (t/m)	Respiratory freq. (r/m)	SpO2 (%)
Normal	60-80	36-37	0	12-24	100-95
Initial	80-90	37.5≥	2-3	25≥	92-90
Transition	90-100	38.5≥	5≥	30≥	90-88
Danger	100-140	38.5≥	10≥	35≥	88-85
Severe	150≥	40≥	10≥	40≥	85<

Once the coding rules were defined, it is possible to establish the weight, which will increase proportionally according to the state; that is, if we have five states, these will be separated by a linear distance given by d defined as: $d = \frac{1}{E_i} \to 0.2$. Moreover, we considered this process as a function of its variables as a disjunction,*i.e.* it is required that only one of the conditions was fulfilled to assign a weight or distance at a moment k.

Therefore, the weights were assigned based on the Bernoulli distribution probability $\sim B(n, p)$ of the rule to be evaluated according to Table 2. This implies that the Bernoulli probability takes the value of the state plus the value of the previous state, increasing this factor per each progression state in the form of a mathematical series as shown below.

$$B_1(1)(k + 0.2) + B_2(2)(k_{n-1} + 0.2) + \dots \\ + B_5(5)(k_{n-1} + 0.2). \quad (20)$$

However, the specific weight of each sample or iteration of the matrix adds the total weight of each of the corresponding parameters; therefore, the specific weight that counts or by which the corresponding T_p state is assigned is denoted as:

$$T_p = \sum_{i=0}^{5} \sim B(i)(k + 0, 2)\forall k = \{1, 2, \dots, 5\}. \quad (21)$$

After the state matrix has been constructed, then it is necessary to know the number of minimum iterations that must be done to evaluate when the matrix will converge in a steady state distribution (stable). Then, this coefficient of ergodicity is calculated according to equation (22).

$$K_{erg} = \frac{1}{2}\left(\max_{i,j=1,\dots,k} \sum_{m=1}^{k} \left| P_{im} - P_{jm} \right| \right) = X. \quad (22)$$

In this specific case, the coefficient of ergodicity provides us with a value of at least 10 iterations to obtain the steady distribution.

b: TRANSITION MATRIX

The state matrix was defined as the matrix that contains in each row the number of times a state E_i is reached, originating from the state E_j. This matrix was normalized according to equation (23).

$$T_N = \frac{p(i,j)}{\sum_{i=0}^{n} p(i,j)}. \tag{23}$$

This matrix has the characteristic of being a probability matrix since each of the columns sums 1 as a total, as will be shown. A matrix of size 5×5 must be obtained; therefore, it is fulfilled that:

$$P_{ij} = P_r \{X_n + 1 = j \mid X_n = i\} \forall i, j \in \mathbb{Z}, n \in \mathbb{N}. \tag{24}$$

It is possible to obtain the transition matrix T as shown in equation (25).

$$T = \begin{pmatrix} p_{11} & p_{12} & p_{13} & p_{14} & p_{15} \\ p_{21} & p_{22} & p_{23} & p_{24} & p_{25} \\ p_{31} & p_{32} & p_{33} & p_{34} & p_{35} \\ p_{41} & p_{42} & p_{43} & p_{44} & p_{45} \\ p_{51} & p_{52} & p_{53} & p_{54} & p_{55} \end{pmatrix}. \tag{25}$$

In this case, given the rapid evolution of the pulmonary conditions caused by COVID-19, it has been considered the use of a Poisson distribution as the probabilistic mode for the disease progression, as based on the previous work of [51].

Therefore, it is established that, in order to move from one state to another, the steps or conditions that are necessary from the point of view of magnitudes are much less than the steps needed to return to the previous step or a lower one given the recovery processes that a COVID-19 patient must face. In other words, when a patient affected by COVID-19 enters a pneumonia state corresponding to state 3, it is then very difficult to go back to the previous state given the inflammatory and bacterial processes developing in the lungs [62]. Thus, the time needed to reach this state is less than the time required to return to the previous step, which supports the use of this type of probabilistic distribution.

The criteria for the generation of the transition matrix is given by the following probability distributions, whose parameters are those limit parameters for the transition to the next state, with E_i being the state based on the parameters.

For the state probabilities, the following values are given:

- $E_1 \Rightarrow P(E_1) = \lambda e^{-\lambda x} \forall x \geq 0$, con $\lambda = 0.2$ & $\sigma = 0.225$,
- $E_2 \Rightarrow P(E_2) = \lambda e^{-\lambda x} \forall x \geq 0$, con $\lambda = 0.2$ & $\sigma = 0.154$,
- $E_3 \Rightarrow P(E_3) = \lambda e^{-\lambda x} \forall x \geq 0$, con $\lambda = 0.2$ & $\sigma = 0.155$,
- $E_4 \Rightarrow P(E_4) = \lambda e^{-\lambda x} \forall x \geq 0$, con $\lambda = 0.2$ & $\sigma = 0.257$,
- $E_5 \Rightarrow P(E_5) = \lambda e^{-\lambda x} \forall x \geq 0$, con $\lambda = 0.2$ & $\sigma = 0.161$.

With this, the transition matrix takes the values as shown in equation (26).

$$T = \begin{pmatrix} 0.026 & 0.028 & 0.379 & 0.241 & 0.324 \\ 0.168 & 0.121 & 0.167 & 0.262 & 0.281 \\ 0.312 & 0.128 & 0.131 & 0.362 & 0.067 \\ 0.018 & 0.538 & 0.302 & 0.089 & 0.042 \\ 0.109 & 0.408 & 0.270 & 0.011 & 0.202 \end{pmatrix}. \tag{26}$$

Taking into account the above, it was possible to determine the probability of a change in state, which together could be represented as the dynamics shown in the finite-state machine of Fig. 4.

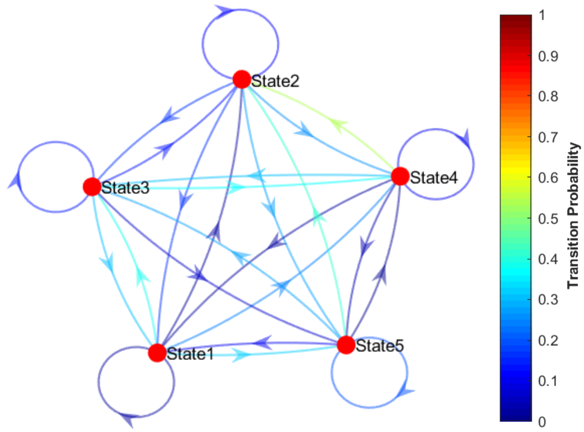

FIGURE 4. State diagram for the probabilities of state transition.

Finally, regarding the modeling process, the steady distribution of the defined chain was known through the calculation of the limit of the transition matrix T raised to the power of time k when the latter tends to be infinite. In this paper, π is the steady distribution and its mathematical expression is as follows:

$$\pi = \lim_{k\to\infty} A^k = \lim_{k\to\infty} S \cdot D^k \cdot S^{-1}. \tag{27}$$

To calculate this limit, a matrix of eigenvectors S must be obtained from the transition matrix T from which the diagonal matrix of eigenvectors D can be obtained; and finally, the inverse matrix of S is calculated as S^{-1}. Since time k tends to be infinite, its value was arbitrarily established as $k = 800$, thus setting 800 iterations of the 10 that are needed to reach convergence, which were corroborated with the mean value.

c: METHODOLOGY FOR VARIABLE HEART RATE

The variability of the heart rate is a very important parameter that will show us how the variability in the short- and long-term in cardiac frequency will reflect the vagal and sympathetic functions of the autonomous neural system. Therefore, heart rate variability can serve as a diagnostic tool in clinical scenarios characterized by dysfunction of the autonomic nervous system [63], which can even be correlated with parameters such as SpO2. This is the reason why this parameter will be widely monitored and framed within the limits given by [63] and specified for these cases [51].

d: TIME ANALYSIS

Time analysis is based on different parameters that can be obtained in two different ways, i.e., from the measurements of R-R intervals or the difference between said intervals. This procedure is exemplified in Fig. 5. If measurements of the

"R" intervals of the QRS complex in an ECG are taken [64], it is possible to establish $\Delta t = R_2 - R_1$, thus obtaining the variables mentioned in the following subsections.

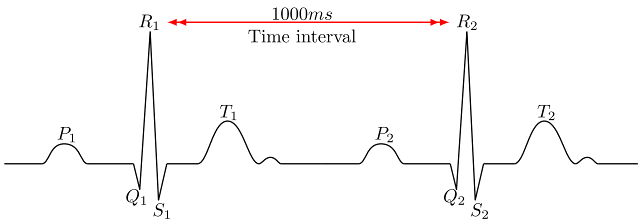

FIGURE 5. **Establishment of a Δt differential from "R" peaks in an ECG.**

- **Average R-R (ms):** It is the mean of the R-R intervals, i.e., the mean of the differences of the vector data V.

$$\Delta v_{BPM}(i) = R(n) - R(n-1),$$
$$(R-R)_{mean} = \frac{\sum_{i=1}^{n} \Delta v_{BPM}(i)}{n} \qquad \forall n \in \mathbb{Z}. \tag{28}$$

- **SDNN (ms):**The standard deviation of all the R-R intervals. This variable shows the variation at short and long periods regarding variation in the R-R intervals (HRV).

$$SDNN = \sqrt{\frac{1}{n-1}\sum_{i=1}^{n}(v_{BPM}(i) - \overline{v_{BPM}})^2}, \tag{29}$$

where $v_{BPM}(i)$ will be the observed values for vector V regarding the mean value of the same $\overline{v_{BPM}}$.
- NN50 It is the number of adjacent intervals that vary for more than 50 ms.

$$NN50_i = 1 \qquad \forall \Delta v_{BPM}(i) > 50ms,$$
$$NN50 = \sum_{i=1}^{n} \frac{pNN50(i)}{n} \qquad \forall n \in \mathbb{Z}. \tag{30}$$

- **pNN50 (%):** It is the number of adjacent intervals that vary for more than 50 ms expressed as a percentage.

$$pNN50_i = 1 \ \ \forall \Delta v_{BPM}(i) > 50ms,$$
$$pNN50 = \sum_{i=1}^{n} \frac{pNN50(i)}{n} 100 \quad \forall n \in \mathbb{Z}. \tag{31}$$

- **rMSSD (ms):**Corresponds to the union of the adjacent R-R intervals. Provides an indicator of vagal heart control (parasympathetic tone).

$$rMSSD = \sqrt{\frac{\sum_{i=1}^{n-1}(\Delta v_{BPM})^2}{n-1}} \forall n \in \mathbb{Z}, \tag{32}$$

Therefore, using the algorithm proposed by [64] and [65], it is possible to obtain these data only by generating the input vector V as already mentioned. This algorithm works by detecting the "R" peaks and calculating the difference in trajectory or time between them, conforming the vector V.

An equivalence in the trajectory with respect to the elapsing time $X \equiv t$ is contemplated as:

$$v_{BPM}(t) = \frac{dx}{dt}. \tag{33}$$

For $v_{BPM}(t)$ as the heart rate speed, x will be the distance covered by the peaks R_1 and R_2 according to Fig. 5. Discretely, a time window can be established for sampling $\Delta t = t_2 - t_1$ where the speed vector V is defined, which contains a known time window to obtain at least 6 "R" peaks according to [66]. Each speed differential and data vector V for HRV is obtained as:

$$v_{BPM}(t) \approx \frac{\Delta x}{\Delta t},$$
$$v_{BPM} = \frac{x_2 - x_1}{t_2 - t_1}$$
$$V = [(v_{BPM}(1), v_{BPM}(2), \ldots, v_{BPM}(n)] \forall n \in \mathbb{Z}. \tag{34}$$

The above is experimentally applied to an ECG of three samples [64].

e: CORE BODY TEMPERATURE

Core body temperature allows us to establish the metabolic relationship in the human body as a function of changes in ambient temperature and intensity of the performed activity (the latter depends on the patient's status). Therefore, the reaction between temperature and viral (including COVID-19) [67] or bacterial affections delivers a good index of the inflammatory processes that may occur in the body. This is why, based on the recommendations of [68], some important parameters have been established for temperature measurement, especially in specific body zones where the measurement can be taken. These bands will determine the statuses that must be analyzed in the Markovian process model to be established.

It has been established that the permissible or normal levels of body temperature in a healthy person, according to [69], correspond to levels that may vary between 97.8°F (36.5°C) and 99°F (37.2°C). During the day, the value can reach a maximum of 37.2°C between 6 and 10 pm, and it drops slowly until the minimum value during 2 to 4 am.

To establish a proper temperature measurement, the measured body zone must be thermoneutral (constant temperature), and the measurement period should last for at least 5 minutes, to ensure the elimination of the thermal inertia component in the sensor. To perform this task, the following circuit of Fig. 6 has been set, wherein the basic connection of the thermistor can be seen. Performance parameters can be obtained as follows.

It can be known from the output voltage to the V_{out} conditioning and ADC circuit that:

$$V_{out} = \frac{R2}{R1 + R2} V_{cc}. \tag{35}$$

For which it is necessary to know $R2$ as a function of the voltage that will be digitalized and its conversion, given by the parameters of V_{adc} and the maximum scale factor

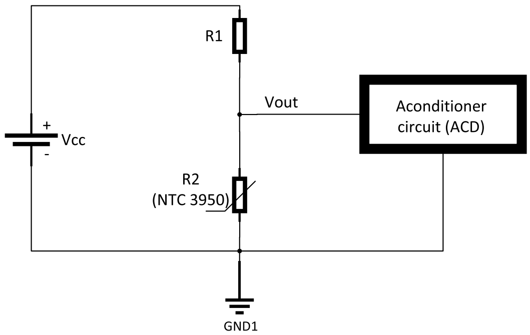

FIGURE 6. Thermistor circuit. Estimation of parameters.

1023, considering a basic conversion of 4 bits. In addition, we consider $R1 = 100k\Omega$.

$$V_{out} = \frac{R2}{R1 + R2} V_{cc},$$
$$R2 = \frac{V_{out} R1}{V_{cc} - V_{out}} = \frac{V_{adc}(100k\Omega)}{1023 - V_{adc}}. \tag{36}$$

Now, the Steinhart-Hart equation is used to perform the conversion to temperature units:

$$\frac{1}{T} = \frac{1}{T_0} + \frac{1}{B} \ln\left(\frac{R}{R_0}\right), \tag{37}$$

wherein T is the temperature measured in $°K$, $T0$ is the nominal temperature of the NTC at $25°C$, B is the constant value $3950 \pm 1\%$, R is the nominal resistance $100k\Omega$, and $R0$ is the calculated series resistance.

Taking into account the above, the sensor arrangement comprises three thermistors which were located in the axillary zone. In this sense, the mean value measured by these three transducers provides the continuous temperature of that body zone [70], [71], as shown in Fig. 7.

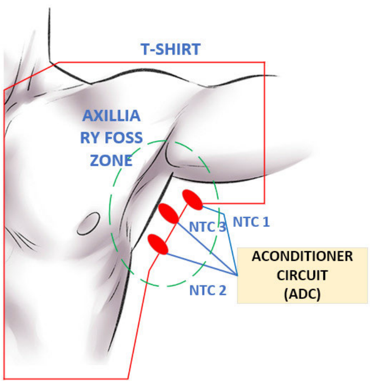

FIGURE 7. Set of NTC thermistors in the axillary zone.

f: COUGH COUNTER, RESPIRATORY FRECUENCY

According to [72], the pattern of cough caused by COVID-19 is dry and persistent. A dry cough or non-productive cough does not produce expectoration and it can impede a person to breath normally. Thus, there is a correlation between HRV and SpO2. In fact, this symptom is usually accompanied by the feeling of shortness of breath; and if it coincides with fever, a key symptom in patients with COVID-19, the evolution of the disease can be established.

In this section, several variables have the same acquisition principle are grouped. These variables correspond to cough count, respiratory frequency and body position detection [70], [73]. The cough count is an important variable to consider in the progress of patients infected with COVID-19. The objective is to measure cough patterns over a period of time T by using MEM inertial sensors in a patient. When a patient coughs, it is possible to measure a change in acceleration of an accelerometer placed in the parathyroid area of a patient. Then, it is possible to detect a pattern related to a ''dry cough'' as a function of the amplitude of the measured variation, as seen in Fig. 8.

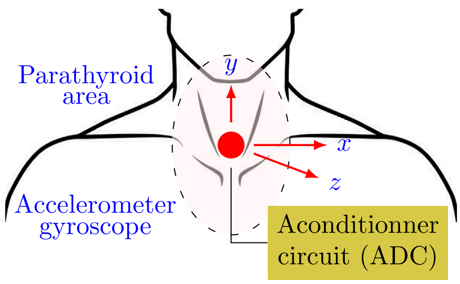

FIGURE 8. Location of MEM sensors in the parathyroid area.

To obtain this parameter, a three-axis accelerometer (as shown in Fig. 8) was used, which detects the acceleration applied in the parathyroid zone when there is movement or coughing occurs. Since ''dry cough'' is a cough that is produced with greater strength, it has a relatively similar duration per each episode; therefore, a pattern can be recognized and compared to obtain a frequency of occurrence for this event.

The parameter of respiratory frequency will also be a patient status indicator, concomitantly representing the state of SpO2 and the affection status of the respiratory system in a COVID-19 patient.

Similar to the previous case, the acceleration measurement was used to establish a pattern of identification of the breathing rhythm of the patient; but the MEMs were incorporated in the xyphoid apophysis area, wherein the deformation caused by breathing was measured per time unit, thus generating the corresponding pattern. The sensor location is shown in Fig. 9.

Regarding counting, each time window has a time T as the experiment duration. As mentioned, the highest peaks were obtained; therefore, a breath was established every two peaks over the total of T period, as shown in the equation (38) below.

$$p(i) \xrightarrow[rel]{max} Si, \forall x = a, p(a) \geqslant a,$$
$$C_i = [p(i), p(i+1)],$$
$$CR = \frac{1}{T} \sum_{i=0}^{n} C_i. \tag{38}$$

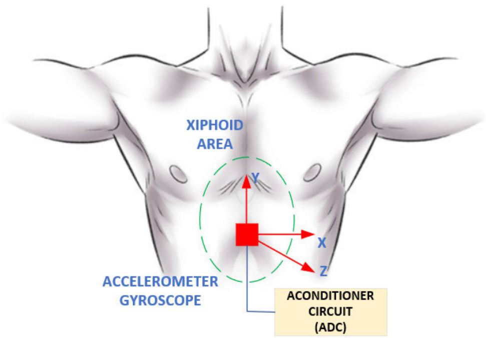

FIGURE 9. **MEM sensors located in xyphoid apophysis.**

g: MEMs

As noted, MEMs sensors, being inertial sensors, sense and measure the effects of gravity at a reference point at both angular and linear levels with extremely high accuracy, permit the quantification of change at a reference point, effectively recording the dynamics of, essentially, what occurs when breathing and coughing [101].

The chosen sensors have the following main features:

- 3-axis accelerometer, configurable to ±2g, ±4g, ±8g, ±16g. The one being used in the ±2g range, suitable range for smooth movements such as breathing and coughing.
- 3-axis gyroscope, configurable up to ±250 degrees/s (ideal for ruling out major torso movements).
- Sampling frequency: up to 1 kHz, typically used between 50-100 Hz for this type of application.

The selection of these sensors, basically covers very important characteristics in the detection of the mentioned variables such as:

- Good sensitivity: An accelerometer of ±2g is acceptable for the detection of smooth movements such as thoracic expansion and contraction, since accelerations will be low.
- Proprietary signal: The movement of the xiphoid process during the act of breathing which follows an oscillatory pattern and can therefore be captured as a periodic signal.
- Non-invasive and portable: This type of solution can be integrated into clothing or straps, making it ideal for continuous monitoring.

Some important limitations that this type of transducer or sensor technology possesses are a function of the dynamics of the environment itself, of which we can mention:

- Signal noise / spurious movement Body movements other than breathing (walking, talking, turning in bed, etc.) introduce a lot of noise that can exceed the thresholds of the signals of interest.
- Accelerometer accuracy (±2g) This range is sensitive, so it is highly susceptible to sudden movements of the subject under study, generating unwanted saturations in the measurements, which would be reflected in the resulting signals, generating loss of basic information.
- Indirect frequency detection Since acceleration (and rotation if you use the gyroscope) is strictly speaking measured for the detection of the mentioned events, it is required to derive a frequency pattern with a known dispersion or characteristic, which makes necessary the use of pre-processors of the data acquired from the accelerometer, which involves Integrating and filtering noisy signals. Segment respiratory cycles correctly. Apply advanced filtering techniques to compensate for changes in the subject's position (reference to the individual's center of mass).
- Transducer (sensor) location and fixation The position of the sensor in the parathyroid and xiphoid areas must be consistent and firm so that it does not move during use. The coupling with the body greatly affects the quality of the signal (poor positioning introduces false positives and parasitic frequencies and noise in the sensors).This implies that for each use a pre-calibration of the sensors should be performed, to obtain a reference of where the sensor is located, and thus be able to compensate for postural changes through an offset vector.

In order to obtain a substantial improvement in the problems inherent to the aforementioned technology, and considering the benefits of its use, we have proceeded to the search for algorithms that allow a solution to the problems associated with the application of the technology and not to the variables, in order to obtain a uniform solution of this. The focused solutions covered two crucial points. The first one associated to the adaptability of the measurement based on the required pattern and the second one associated to the adaptability but of the amplitude based

For the first point, it has been decided to apply an adaptive Kalman filter, which will be able to establish the breathing pattern and cough frequency.

The system model is given by equation 39.

$$x_k = Ax_{k-1} + w_k, \tag{39}$$

where x_k True state at time k (acceleration we want to estimate), A is the transition state matrix (for this case will be considered 1 means the features of the dynamics of the accelerometer it does not change) w_k noise at the sampling process (or Q covariance).

Regarding the observation or measuring model, this is defined in the equation 40.

$$z_k = Hx_k + v_k, \tag{40}$$

where z_k Measured or observation sampling, H is the observation matrix ($H = 1$ for this case, because the measurement performed was directly made) v_k

The design of the filter, based on its operating conditions, has different phases, the first of which corresponds to the prediction phase, given by the following equation 41.

$$\hat{x}_k^- = A\hat{x}_{k-1},$$
$$\hat{P}_k^- = AP_{k-1} + A^T + Q, \tag{41}$$

where $\hat{x}_k^-$ is the predicted or "a priori" state, $\hat{P}_k^-$ is the covariance error predicted or "a priori".

For the update or subsequent phase for the filter output parameter update, it is modeled with the equation 42

$$K_k = \hat{P}_k^- H^T \left(HP_k^- H^T + R\right)^{-1},$$
$$\hat{x}_k = \hat{x}_k^- + K_k \left(z_k - H\hat{x}_k^-\right),$$
$$P_k = (I - K_k H)\, P_k^-, \tag{42}$$

where K_k Kalman gain (determines the likelihood level of the next measurement or sample) $\hat{x}_k$ Estimated filtered system output P_k it is the covariance of the filter or system output.

The management of saturation will be given by the comparison in a desired range of amplitudes of the breathing or coughing signal. This threshold will be obtained from a period of time $z(k)$ for which, from statistical sampling parameters such as the mean and standard deviation, the detection of the saturation will be carried out as follows

$$\mu = \frac{1}{N}\sum_{i=0}^{N}(z_i),$$
$$\sigma = \sqrt{\frac{1}{N}\sum_{i=0}^{N}(z_i - \mu)^2},$$
$$\text{Satured Signal} \Rightarrow |z_k - \mu| > \lambda_\sigma, \tag{43}$$

where λ is the signal threshold considered in a discrete period of time $z(k)$, here the saturated points will be replaced by $\hat{x}_k$

The design and implementation of this filter can be physically interpreted as:

- The actual acceleration applied to the MEMS follows a constant pattern with small variations (or process noise Q) for a small time interval as a function of its sampling rate.
- Measurements have noise (R).
- Saturation in the output signal are outliers that deviate significantly from normal behavior (Outliers).

Regarding the filter gain or Kalman gain K_k acts as a weighting factor between:

- Model prediction $\hat{x}_k^-$
- New sample or measurement z_k

When R is large relative to P_k^-, K_k becomes small, making the filter converge its parameters or rely on its prediction rather than on the measurement (useful to discard saturation).

Saturation corrections are detected as a pair of the vector S where:

$$\hat{x}_k^{\text{corrected}} = \begin{cases} \hat{x}_k & \text{if } k \in S \\ z_k & \text{other cases.} \end{cases} \tag{44}$$

Figure 10 shows the effectiveness of the filter against saturation due to the effects of a movement of the subject under study, here is shown the noise filtering and the reconstruction of the signal by saturation levels, from the signal reference data. The detection of the saturated signals are replaced by the signals of the pattern in the same time window, dispersion in this window and sample average, with this a robust and intelligent filtering is obtained, which allows to have a greater reliability of the signal under study. This clearly applies to the two signals cough and respiration.

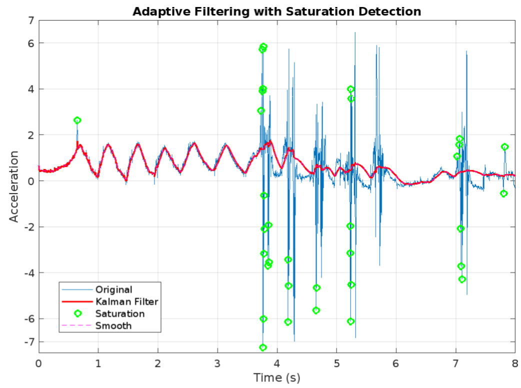

FIGURE 10. Breathing frequency filtered signal, based on adaptive Kalman filter and detection of acceleration saturation anomalies.

h: SpO2

SpO2 may be defined as per the following components: "S" indicates saturation; "p" refers to percent, and O2 means oxygen. The acronym is a measurement of the amount of oxygen fixed to hemoglobin in red blood cells of the circulatory system. In summary, this parameter indicates the amount of oxygen transported by red blood cells. As a measured value, the SPO2 points to the degree of respiratory efficiency of a patient and how oxygen is transported through the body. SpO2 uses a percentage value to indicate the said measurement, such as 96% for a healthy adult.

In this case, the classification of this parameter was established using the values indicated in Table 3.

TABLE 3. Tabulation of SpO2 limits criteria.

SpO2	PaO2	Range
97% Saturation	97% PaO2	Normal
90% Saturation	60% PaO2	Danger
80% Saturation	45% PaO2	Severe Hypoxia

To perform these measurements, optical pulse oximetry was used as a non-invasive method to determine SpO2. Its functioning is based on the fact that hemoglobin (Hb) and saturated hemoglobin (oxyhemoglobin, HbO2) have different light absorption coefficients for different wavelengths.

The SoC solution to be used includes the red (660 nm) and infrared (880 nm), as well as photodiodes to measure the reflected light, and an ADC of 18 bits and frequency sample of 50 sps (samples per second) at 3200 sps. This process is represented in Figure 11. However, the graphs obtained in this process show typical variability in relation to the normal saturation limits, as well as, for example, the beginning of a hypoxia event, as can be seen in the graph of Figure 11.

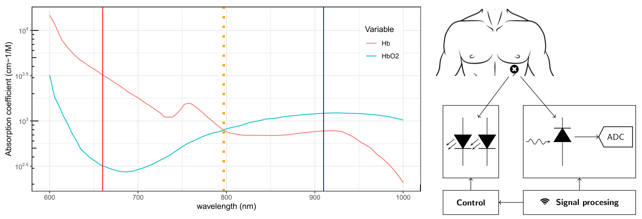

FIGURE 11. **Measurement of SpO2 based on spectrography.**

D. BIOMEDICAL SENSOR CALIBRATION

The biometric sensors used focused on measuring HRV, SpO2, Cough Frequency, and Respiratory Rate variables. All these sensors are based on SoC (System on Chip) solutions, which means integrated microelectronic systems designed for the development of transduction stages, signal conditioning, and output in standardized signals (such as synchronous serial communication signals, analog signals like 0-3.3 V, etc.).

However, the sensors used were divided into two technologies: one based on standard instruments certified under ISO-13485 [74], ensuring their calibration according to standardized patterns, such as ECG sensors and SpO2 sensors.

In terms of sensors, they focused on measuring the frequency of coughing and the frequency of breath. Those were developed based on MEMS (Microelectromechanical system) technology. That is a mean instrument based on the mechanical behavior of the gravity force, with accelerometers and angular velocity from a reference point with 6 deegres of freedom, as was mentioned previously.

These latter devices require calibration due to their high sensitivity to movement and high-frequency motion interference. Therefore, their calibration procedure is based on comparison with more complex instruments that measure changes in the thoracic region and the xiphoid apophysis.

The process of determining the sensor caliber considers the following:

Static Calibration: The accelerometer SoC is placed in several known orientations (e.g., 0°, 90°, 180°, 270°) and the outputs are recorded. The samples are compared with theoretical values of gravity (1 g, −1 g, 0 g, etc.). Compensation for deviations is adjusted in the accelerometer by offset and sensitivity adjustments to minimize the error between the readings and the theoretical values.

Dynamic Calibration: A controlled motion system, such as a shaker table or robotic arm, is used to apply known accelerations. The samples are recorded and compared with the expected values (datasheet values).

Temperature Compensation: If the instrument is used at different temperatures, tests are carried out over a range of temperatures, and the parameters are adjusted to compensate for any thermal drift, in this case just for a limited range of $[0\ 20]°C$.

Given the data provided at the dynamic and static calibration of the MEMS. an static validation was performed based on the error distribution for each axys of the accelerometer. The experiment was performed with 100 samples, each sample was aquired with a period of $1ms$. The accelerometer was oriented in a known direction, defined by the position to be used in the detection of physiological events. The position is given by the equation (45) where P is the resultant of the position where the action of the gravity affects the accelerometer.

$$P = \begin{bmatrix} \widehat{x} & \widehat{y} & \widehat{z} \\ 0^0 & 0^0 & 90^0 \end{bmatrix} = \begin{bmatrix} \widehat{x} & \widehat{y} & \widehat{z} \\ 0\frac{m}{s^2} & 0\frac{m}{s^2} & 9.8\frac{m}{s^2} \end{bmatrix} \tag{45}$$

This vector will be compared with the samples obtained from the accelerometer vector $P_s(t)$ and the theoretical values $P(t)$. The deviation or error $e(t)$ it is defined as $e(t) = P(t) - P_s(t)$. Considering as $e(t)$ as a variable to minimize and considering as the mean value as the DC signal, and this is the same to offset of the signal, it is possible to define as the expression (46). Where T it is the time window of the experiment. Since the accelerometer samples has 3 directions means one level o DC component for each direction. The expression shows how the offset vector is conformed, and the values obtained are shown at the same equation (46).

$$\begin{aligned} e_{DC} = e_{mean} &= \frac{1}{T}\int_0^t e(t)\mathrm{d}t \approx e_{offset}(x, y, z) \\ &= \frac{1}{n}\sum_{i=0}^{n} e_{(x,y,z)}\,[i] \\ e = \begin{pmatrix} e_x \\ e_y \\ e_z \end{pmatrix} &= \begin{pmatrix} 0.011 \\ 0.009 \\ 0.98 \end{pmatrix} [\frac{m}{s^2}] \end{aligned} \tag{46}$$

Additionally, it is strongly necessary to adjust the sensitivity at each directions of the obtained signals of the accelerometer. The sensitivity it is defined by:

$$\begin{aligned} e_{sensivity}(x, y, z) &= \frac{1}{n}\left(\sum_{i=0}^{n} \frac{P_{s(x,y,z)}[i]}{P_{(x,y,z)}[i]}\right) \\ e_{sensivity} &= \begin{pmatrix} e_{sensitivy(x)} \\ e_{sensitivity(y)} \\ e_{sensitivity(z)} \end{pmatrix} = \begin{pmatrix} 0.9040 \\ 1.1424 \\ 1.0006 \end{pmatrix} \end{aligned} \tag{47}$$

Finally the adjusted value and probability distribution of the error are shown at the graphics shown in the Fig. 12 achieving a minimal error at the accelerometer.

E. FORTH LAYER: VLP AND EVOLUTION OF COVID-19

1) VLP

The localization process uses trilateration to determine the 3D coordinates of the receiver based on the distances calculated from each LED. This process builds on the previously defined relationships between the received power, the geometry of the system, and the channel characteristics.

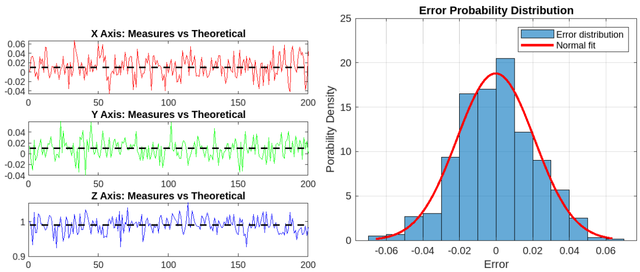

FIGURE 12. **Axis signals and error probability distribution.**

The trilateration method involves solving for the unknown coordinates of the receiver by minimizing the error between the measured received power and the power predicted by the VLC channel model. Given the non-linear nature of the problem, an optimization approach is necessary.

The error function, which quantifies the difference between the received power P_{LOSij} and the expected power calculated using the known positions of the LEDs and the estimated position of the receiver, is defined as:

$$f_{3d}(x_{pi}, y_{pi}, z_{pi}) = \sum_{i=1}^{3}\left(\frac{A_j(m_i+1)}{2\pi}T_j(\psi_i)g_j(\psi_i)P_{ti}\frac{(z_{pi}-z_i)^{m_i+1}}{d_{pi}^{m_i+3}} - P_{LOSij}\right)^2 \tag{48}$$

This equation is derived from the principles established in the VLC system model. The received power is expressed as a function of the angles of incidence, the VLC channel characteristics, and the distance between each LED and the receiver. To accurately determine the receiver's position, the objective is to minimize the error function.

To achieve the proposed goal, the PSO algorithm is employed to solve this optimization problem. This technique is widely used for problem involving continues and multi-dimensional search spaces. In this context, each particle int PSO algorithm represents a possible solution. In this case, each particle represents one possible position of the receiver. Then, while the algorithm iterates, the particles adjust their locations based on their own experiences and information shared by neighbors particles, converging toward coordinates that minimize the error function. The result of the algorithm is the position that yields the lowest value of the objective function.

2) EVOLUTION OF COVID-19

To reduce computational complexity, this paper assumes that future states depend solely on the current state. For example, multi-state survival analysis often reveals the existence of transient dependencies on previous events or multiple time scales, which can introduce biases if not properly accounted. Moreover, the complexity of real-world data can pose challenges in parameter estimation and model validation, requiring advanced computational techniques and sensitivity analysis to ensure accurate predictions [75], [76]. This is why Markov chains emerge as a method for solving systems in discrete times or states, as mentioned, without the dependence on future states for making predictions.

V. RESULTS

A. SETUP AND PARAMETERS OF THE SIMULATION

First, the tests were conducted in a room with dimensions $(5 \times 5 \times 3)$ meters, using Python along with relevant libraries such as NumPy and SciPy for numerical computations and Matplotlib for visualizations. Three LEDs with known positions were used: LED_1 is located at (1, 2, 3) meters, the LED_2 at (1, 4, 3) meters, and the LED_3 at (4, 3, 3) meters. In addition, 100 receiver locations were defined, distributed across the length, width, and height of the room, to thoroughly test and analyze the system's performance.

To evaluate the performance of the proposed system, various simulations were executed. The first phase consists of test different values for PSO parameters with the objective of finding a configuration that provides the result with the lowest error. Then, the optimal number of particles is determined to balance precision and the algorithm's execution time. Finally, the number of iterations is evaluated to determine an optimal value based on convergence.

It is important to note that the algorithm's performance in terms of accuracy was measured by the error between the estimated position and the actual position of the target. This is expressed as follows:

$$d_{error} = \sqrt{(x_t - x_r)^2 + (y_t - y_r)^2 + (z_t - z_r)^2}. \tag{49}$$

The characteristics of the simulated system and the environment in which it operates are defined according to the values shown in Table 4 [77], [78], [79], [80], [81], [82], [83].

TABLE 4. **Positioning system parameters.**

VLC Simulation Parameters	Values
Dimensions of the room $(w \times l \times h)$ (m)	$(5 \times 5 \times 3)$
Coordinates of the $LEDs(x_i, y_i, z_i)$(m)	$LED_1 = (1,2,3)m$, $LED_2 = (1,4,3)m$, $LED_3 = (4,3,3)m$
Power of each LED_i (W)	8
Gain of each optical filter, $g_j(\psi_i)$	Unity Gain
Effective area of each PD_j, A_j (m^2)	10^{-4}
Gain of each optical concentrator, g_j	Unity Gain
Photoelectric conversion efficiency $(\frac{A}{W})$	0.54
FoV of each PD_j, Ψ_j (°)	90°
Lambertian order, m_i	1
Equivalent noise bandwidth (MHz)	100
PSO parameters	
Initial particle velocity, v_t	$\mathcal{U}$[0,1]
Cognitive factor, c_1	[0 - 3]
Social factor, c_2	[0 - 3]
Cognitive random parameter, r_1	$\mathcal{U}$[0,1]
Social random parameter, r_2	$\mathcal{U}$[0,1]
Iterations	[1 - 500]
Particles	[25 - 1500]
Inertia weight, w	[0 - 2]

B. COGNITIVE AND SOCIAL FACTORS VARIATION

In this section, we analyze the impact of the acceleration coefficients of the cognitive and social factors (c_1 and c_2, respectively) on the system's average localization error. To this end, multiple simulations were performed that varied both parameters in the range of [0, 3], while keeping the other parameters of the PSO algorithm constant.

Fig. 13 shows the results of the average localization error as a function of the values of c_1 and c_2. The horizontal axis represents the acceleration coefficient values, and the vertical axis indicates the average error in centimeters.

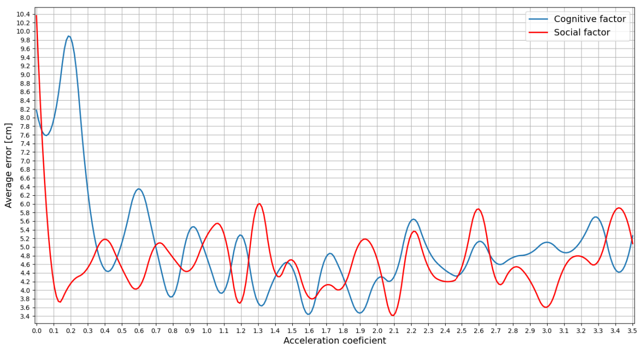

FIGURE 13. Average localization error [cm] vs $c1$ and $c2$ values.

The blue curve in Fig. 13 represents the variation in average error as a function of the cognitive factor c_1. It can be seen that for values of c_1 between 0 and 0.3, the average error decreases rapidly, reaching a minimum of approximately 0.3. As c_1 continues to increase from 0.3 to 1.0, the average error fluctuates but remains relatively low. Between 1.0 and 2.0, several error peaks are observed, while the error decreases and stabilizes around $c_1 = 1.6$ and $c_1 = 1.9$, where optimal values are found to achieve the highest precision.

The red curve in Fig. 13 shows the variation in average error as a function of the social factor c_2. It can be seen that for values of c_2 between 0 and 0.3, the average error decreases significantly, reaching a minimum of approximately 0.3. As c_2 increases from 0.3 to 1.0, the average error fluctuates slightly but remains low. Between 1.0 and 2.0, several error peaks similar to those of the cognitive factor are observed. The optimal c_2 values to achieve the lowest error are found around 2.1 and 3.0.

The analysis shows that both factors significantly impact the localization error. A proper balance between the values of c_1 and c_2 is crucial to optimize the performance of the PSO algorithm. A moderate cognitive factor allows particles to improve their positions based on previous experiences, contributing to more accurate localization. An adequate social factor enables the particles to benefit from the collective experience of the swarm, promoting convergence to optimal solutions.

C. INERTIAL WEIGHT VARIATION

In this section, we analyze the impact of the inertial weight (w) on the system's average localization error. To this end, multiple simulations were performed that varied w in the range of [0, 2], while keeping the other parameters of the PSO algorithm constant. Fig. 14 shows the results obtained, where the horizontal axis represents the values w, and the vertical axis indicates the average error in centimeters.

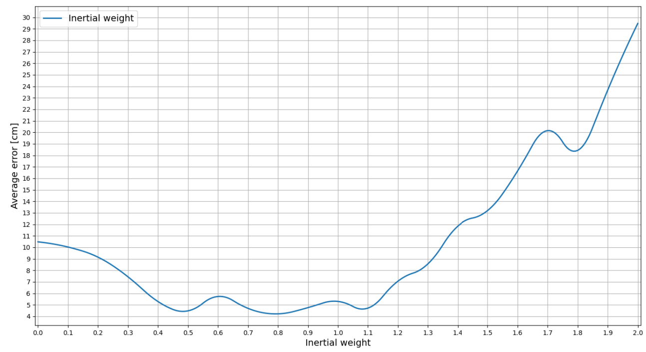

FIGURE 14. Localization error [cm] vs Inertial weight.

Fig. 14 presents how average localization error varies with the inertial weight. In first place, when w is in 0 and 0.5 range, the average error decreases reaching a minimum of 0.5, approximately, where the system has 4.5 cm of precision. Observing all the graph, this value for w is the optimal configuration due the lowest error.

For w values between 0 and 0.5, the error decreases until $w = 0.5$. Then, the average error fluctuates in the range 4 and 6 cm. However, when w is bigger than 1, the precision decreases to the maximum value of error. Taking into consideration this, we can conclude that the optimal range for w is between 0.5 and 1. This analysis confirms that the inertial weight is fundamental to the performance of the PSO algorithm. Careful selection of w is important for precision in the localization process. Higher values of w (greater than 1) and lower inertial weights (less than 0.5) show an increase in error.

D. PSO PARAMETERS COMBINATION

To evaluate how the algorithm variables interact, the optimal values of the PSO parameter w, c_1, and c_2 obtained from individual tests were combined to assess their combined impact on the average localization error. Table 5 presents the results of the combinations of selected parameters, including the average error and the 50%, 75%, 90% and 100% percentiles. This table shows how different combinations of these parameters affect the accuracy of the localization system. Although some parameters provided higher positioning accuracy when tested individually, their combination reveals that the interaction between parameters plays a crucial role in system performance.

The results shown in Table 5 allow us to emphasize the importance of choosing a parameter combination in

TABLE 5. PSO parameters combination results.

w	c_1	c_2	Error [cm]	50% [cm]	75% [cm]	90% [cm]	100% [cm]
0.5	1.6	2.1	5.05	0.65	2.32	6.30	15.44
0.5	1.6	3.0	4.83	0.69	1.51	5.49	15.08
0.5	1.9	2.1	12.69	0.76	1.95	25.73	35.72
0.5	1.9	3.0	10.17	0.47	1.74	18.55	29.82
0.8	1.6	2.1	4.88	0.50	1.97	14.09	12.90
0.8	1.6	3.0	7.15	0.48	1.80	16.51	20.91
0.8	1.9	2.1	3.24	0.46	1.09	3.91	9.70
0.8	1.9	3.0	3.28	0.56	1.66	4.75	8.96

achieving the desired precision in the localization process. For example, utilizing $w = 0.8$, $c_1 = 1.9$, and $c_2 = 2.1$ results in an average error of 3.24 cm, which yields the lowest value compared to other configurations. Moreover, this combination minimizes the maximum error value. 90% of the measurements are lower than 3.91 cm, while the rest 10% increase the error to 9.70 cm. Similar results are obtained with the setting $w = 0.8$, $c_1 = 1.9$, and $c_2 = 3.0$. On the other hand, $w = 1.5$, $c_1 = 1.6$, and $c_2 = 3.0$, or $w = 0.8$, $c_1 = 1.6$, and $c_2 = 3.0$ results in the higher errors compared to the rest of the configurations.

E. NUMBER OF PARTICLES VARIATION

This section analyze the impact of the number of particles on the average localization error and the execution time of the PSO algorithm. To this end, multiple simulations were conducted that varied the number of particles in the range of 25 to 1500, while keeping other algorithm parameters constant. Specifically, the optimal values of the PSO parameters previously found were used: $w = 0.8$, $c_1 = 1.9$, and $c_2 = 2.1$

Figs. 15 and 16 show the results obtained. The first image presents the relationship between the average localization error and the number of particles used. The maximum average error is obtained for 50 particles, where the result is 40 cm, approximately. But incrementing the number of particles, the error is reducted. Around 700 particles and higher values, the precision is stagnant in fluctuations between 2 and 8 cm. In conclusion, adding particles number could outcomes a better precision, but the error correction has limitations. Therefore, it is necessary to balance the quantity of particles considering required precision and computational resources.

Fig. 16 shows the execution time of the algorithm as a function of the number of particles. Here, a direct linear relationship is observed, where the execution time increases consistently with the number of particles. This behavior is expected, as a higher number of particles implies more calculations in each iteration of the PSO algorithm. Although the execution time for 25 particles is approximately 10 ms, this increases to almost 270 ms for 1500 particles.

Analyzing both figures, the behavior of localization error when increasing the number of particles decreases, but the algorithm's execution time grows. For this reason, it is crucial to balance the number of particles and the positioning system performance considering both precision and computational requirements. Using these results, 700 to 1100 particles seem to provide low average error compared to other simulations, and maintain acceptable execution time.

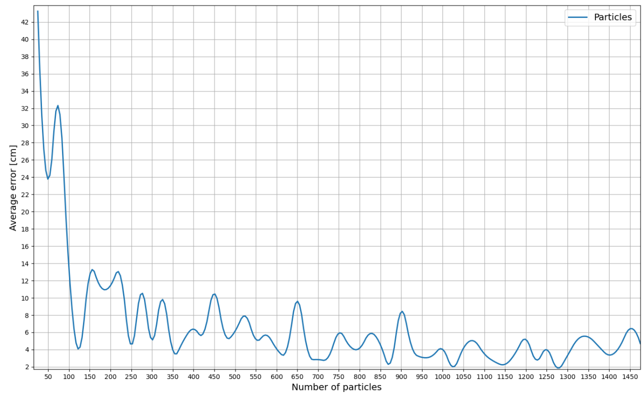

FIGURE 15. Average localization error as a function of the number of particles.

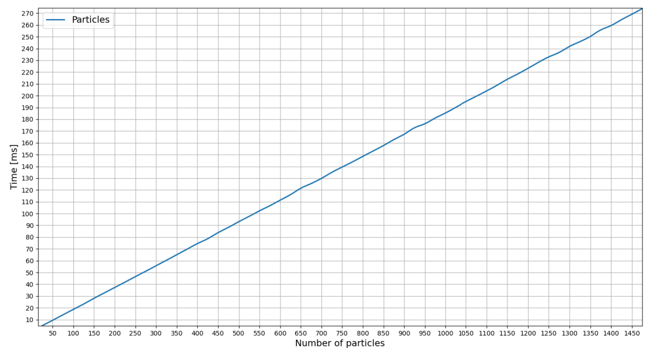

FIGURE 16. Algorithm execution time as a function of the number of particles.

F. COGNITIVE AND SOCIAL FACTORS VARIATION

In this section, we analyze the number of iterations required for the objective function of the PSO algorithm to converge, using the optimal parameters previously determined: $w = 0.8$, $c_1 = 1.9$, $c_2 = 2.1$, and 875 particles. Fig. 17 shows how the value of the objective function changes as the iterations progress.

From Fig. 17 can be observed how the objective function value is affected by the number of iterations in the algorithm execution. The initial value of the function to optimize is, approximately, 10^{-11} in early iterations. Nevertheless, when the iterations are greater than 20, the objective function decreases approaching 0. After 40 iterations, the algorithm converges, and the improvements to objective function value are minimal compared to early phases. For now, setting the number of iterations around this quantity should be sufficient for the proposed system to save computational resources.

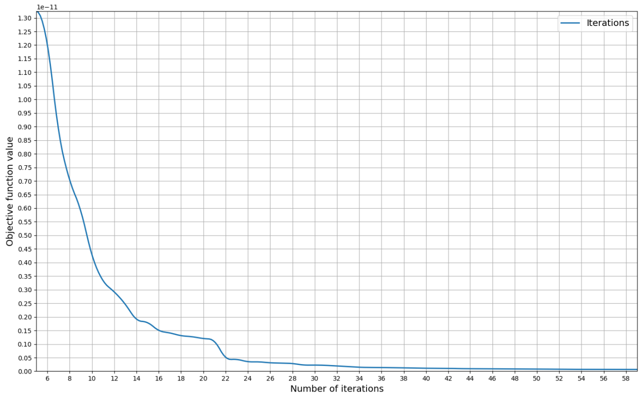

FIGURE 17. **Convergence of the value of the objective function as a function of the number of iterations.**

G. CALIBRATION AND RECOGNITION OF COUGH

In Fig. 18, it can be seen that the main peaks correspond to the generation of dry cough, which is used to properly calibrate the sensor. The average duration of these events is approximately 200 ms, with a mean measured acceleration of 5.58 m/s^2. Based on this information, a characteristic pattern can be established to identify this physiological event. This event is presented in Fig. 18 where the base in acceleration is produced because of the cough, generates peaks of acceleration where the difference of the maximum for each event said the period of the event. In this case for an experiment with a duration of 8 seconds, the event reaches a frequency of 0.2 Hz.

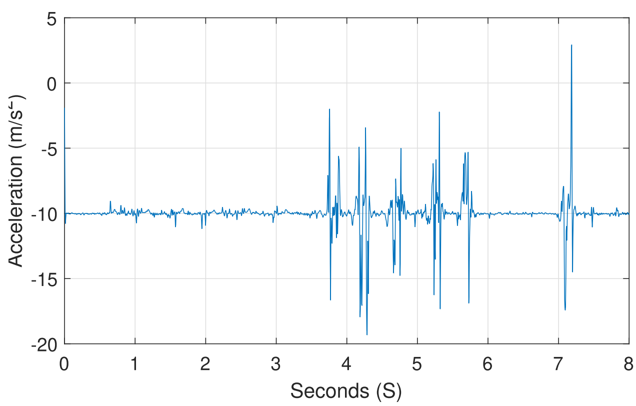

FIGURE 18. **Measurement and recognition of cough.**

H. CALIBRATION AND MEASUREMENT OF RESPIRATORY FREQUENCY

To calibrate the respiratory rate measurements, the following pattern was analyzed, illustrating the clear respiratory cycle depicted in Fig. 19. Each cycle was identified by locating its maximum points, with a time window T defined for the measurement. For accurate signal scaling, gravitational acceleration must be considered, with a conventional value of 9.8 m/s^2. Furthermore, a 16-bit MEMS resolution was used, resulting in a total scale of $R = 2^n$ for $n = 16$, which produces a range of $R = 16384$. The same applies to the cough frecuency sensor. Here, using gravity acceleration, the acceleration was detected in time for each deplexion of the breastbone; in this case, the respiratory frequency was 1.3 breath/min.

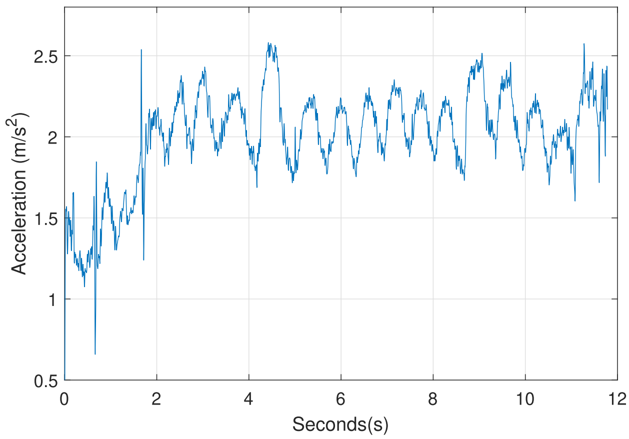

FIGURE 19. **Recognition and measurement of respiratory frequency.**

I. CALIBRATION OF OXIMETER SENSOR

The calibration of the **SoC** solution utilizes red light (660 nm) and infrared light (880 nm), along with photodiodes to detect reflected light, and an 18-bit ADC with a sampling frequency ranging from 50 sps to 3200 sps. This process is illustrated in Fig. 11. However, the graphs obtained in this process show typical variability in relation to the normal saturation limits, as well as, for example, the beginning of a hypoxia event, as can be seen in the graph of Fig. 20.

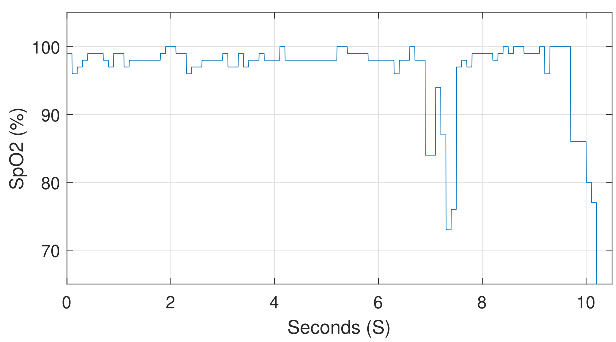

FIGURE 20. **Detection of hypoxia with MEM sensors located in xyphoid apophysis.**

Oxygenated blood absorbs more infrared light, while deoxygenate blood absorbs more red light. In areas of the body where the skin is thin enough and blood vessels are close to the surface, this difference can be exploited to accurately determine the level of oxygen saturation.

J. RESULTS OF THE PROGRESSION OF THE DISEASE

Given the current scenario of a coronavirus-caused pandemic (COVID-19) and the existing safety protocols, it was very difficult to perform a real test of the proposed system in a health institution with infected patient.

However, many health care researchers have put a lot effort and resources into documenting important and critical variables associated with patient stability, as well as those associated with respiratory infections, specifically SARS-Cov-2 virus infections (COVID-19). Most of these public databases have been used to validate the algorithm presented. Among these efforts, we can cite [102], [103], [104] who acquired data associated with their vital signs, including heart rate, oxygen saturation, temperature, among others, which were arranged in time windows until reaching a total of 12 or more hours upon admission to the health service, in addition to categorizing whether they had been subsequently diagnosed with the viral infection. COVID-19. Therefore, the results obtained could be validated with the algorithm presented in terms of the results shown in this proof of concept. A data set for confirmed cases was obtained from the mentioned databases, from which the input data were obtained.

The collected data was associated with 16 different time periods during 5 days. Data were collected at times $k = 1, 2, 3, 4, 5$ during the day and $k = 6, 7, 8, 9, 10$ during the night. With these data, the input data vectors reached dimensions of 100 measurements or 100 elements, each of them with a sampling frequency of 360 Hz for all the parameters. This vector was denoted as A_{in}, which after data processing was built as the following data matrix as represented in Table 6.

TABLE 6. Input data matrix A_{in}.

k	Heart Rate *bpm*	Temp. $^\circ C$	Cough (minute)	Breathing Freq. (minute)	SpO2 %
1	75	36.8	0.1	12	98
2	75	37.0	0.1	18	98
3	75	37.2	0.1	20	97
4	82	37.5	2	21	97
5	85	37.6	2.1	22	96
6	88	38.0	2.5	23	95
7	89	38.3	2.6	25	94
8	90	38.5	3	25	90
9	100	38.5	5	30	90
10	112	39.0	5	35	90
11	134	39.1	8	35	89
12	140	39.2	8	35	89
13	140	39.1	8	38	88
14	140	39.0	10	38	86
15	140	39.0	10	38	86
16	141	39.0	10	40	86

With these data, it was then possible to establish the values for the probability of progression of the disease. For this purpose the hypothesis question was defined, which according to the general objective of this research work, was focused on the probability for disease worsening or to reach a severe state in the patient. Thus, the probability can be expressed as follows.

$$p(k) = A^k p(o) \Rightarrow p(1) = T^1 p(0), \tag{50}$$

wherein $p(k)$ is the probability of occurrence of a fact in a time k based on the initial probability distribution or initial state $p(0)$ and a probability distribution of change in state T.

In this case, the initial states were determined by the state as predicted in Table 7; therefore, the states were binary per each state since the initial state is represented as 100% of probability of being in the said state.

TABLE 7. PSO parameters combination results.

k	Heart Rate *bpm*	Temp. $^\circ C$	Cough (minute)	Breathing Freq. (minute)	SpO2 (%)	State
1	0.25	0.2	0.4	0.2	0.2	1
2	0.25	0.2	0.4	0.2	0.2	1
3	0.25	0.4	0.4	0.2	0.2	1
4	0.4	0.4	0.4	0.2	0.2	2
5	0.4	0.6	0.4	0.2	0.2	2
6	0.4	0.6	0.4	0.2	0.2	2
7	0.4	0.6	0.4	0.4	0.4	2
8	0.4	0.6	0.4	0.4	0.4	2
9	0.6	0.6	0.6	0.6	0.4	3
10	0.8	0.8	0.6	0.8	0.4	3
11	0.8	1	0.8	0.8	0.6	4
12	0.8	1	0.8	0.8	0.6	4
13	0.8	1	0.8	1	0.6	4
14	0.8	0.8	0.8	1	0.8	4
15	0.8	0.8	0.8	1	0.8	4
16	1	0.8	0.8	1	0.8	4

For example, if $p(0) = [1 \ 0 \ 0 \ 0 \ 0]^T$, it means that the initial state of $p(0)$ is the state with probability 100% at time k. In this sense, by processing the data obtained it is possible to define a heat map diagram as in Fig. 21, where the percentage of probability per time k and the values of the parameters as a function of the input data A_{in} are shown according to the above. In order to understand this map, it is necessary to refer to a specific time k. Regarding the states axis, the probability shown at said state corresponds to the probability of permanence in said state; and the following, to the probability of passing to the next state and vice versa.

It can be seen that, throughout the iterations, several very different probabilities can be obtained between each state with respect to time k. This is because each sample or the samples per each parameter were taken at very different times, so there was no continuity in the progression. However, these are consistent among them as a function of the input data with which they were evaluated in the chain.

VI. DISCUSSION

Table 8, presents a detailed analysis of the results obtained in the study, by items of analysis: 1) Cognitive and Social Factors Variation, 2) Inertial weight variation, 3) PSO Parameters Combination, 4) Number of iterations variation, 5) Comparative Analysis of Localization Accuracy, 6) Calibration and measurement of respiratory frequency,

TABLE 8. **Analysis of the results and comparative analysis.**

Items	Analysis	Comparative analysis
Cognitive and Social Factors Variation	The examination of Fig. 13 underscores critical elements. Cognitive and social factors substantially affect localization accuracy. For $0 \leq c_1 \leq 0.3$, the error diminishes significantly. For values of c_1 in the range $0.3 < c_1 \leq 1.0$, the error exhibits minor fluctuations. Optimal values of c_1 are located within the range $1.0 < c_1 \leq 2.0$. The minimal errors are observed at $c_1 = 1.6$ and 1.9. For $c_1 > 2.0$, precision markedly declines. The social element operates in a manner analogous to the cognitive component. For $0 \leq c_2 \leq 0.3$, the error diminishes swiftly. For values of $c_2 > 0.3$, the error stabilizes with negligible changes. The minimal errors are observed for $c_2 = 2.1$ and 3.0. The localization accuracy for c_2 remains unchanged within the range $0 \leq c_2 \leq 0.3$. Optimal values of c_1 and c_2 are essential for precision.	Localization accuracy is influenced more by cognitive and social factors. The PSO algorithm optimization is enhanced by supplementary enhancement strategies. Cognitive and social factors substantially influence the processing of environmental information. The incorporation of adaptive parameter modifications improves algorithmic efficiency and accuracy [84]. The application context is essential for the adaptation of these technologies. Wireless sensor networks require particular modifications for optimal operating efficiency [85], [86].
Inertial weight variation	The research demonstrates precise localization within 0.4 to 1.0. The minimal error peaks occur at $w = 0.5$ and $w = 0.8$. Error escalates for inertia weight levels beyond $w > 1.1$. Adjusting inertia weight guarantees accurate positioning and precision.	While inertia weight is crucial, its efficacy is contingent upon the situation. An appropriately calibrated weight enhances convergence across diverse issues. Tailored techniques facilitate the attainment of optimal outcomes in Particle Swarm Optimization (PSO). Adaptive strategies modify w to enhance the equilibrium between exploration and exploitation. Static methodologies exhibit inflexibility un dynamic optimization endeavors. Strategy selection requires empirical assessment for optimal performance [85], [87].
PSO Parameters Combination	The findings indicate that parameter selection substantially affects localization accuracy. A test determined that $w = 0.8$, $c_1 = 1.9$, and $c_2 = 2.1$ are best values. This combination resulted in an average inaccuracy of 3.24 cm. Ninety percent of samples exhibited accuracy within 3.91 cm. Employing $w = 0.5$ resulted in inaccuracies above 10 cm. Ninety percent of instances exhibited errors over 15 cm. Results demonstrate heightened instability with these parameter selections.	Static tuning is effective in low-variability situations but has constraints. Intricate issues are enhanced by adaptive optimization methodologies [88]. IASPSO dynamically modifies inertia weight and acceleration coefficients [89]. This enhances both exploration and convergence precision in algorithms.
Number of iterations variation	Examining iteration variability diminishes PSO execution duration. This facilitates more effective localization in apps. The method mitigates superfluous utilization of computational resources. Simulation findings indicate that PSO converges following 40 iterations.	Forty iterations enhance performance through particle convergence. The value may be altered by changes in requirements and problem characteristics. The objective function and the environment influence the need for iterations. Computational resources also affect the necessary iterations [90].
Comparative Analysis of Localization Accuracy	In [6], Particle Swarm Optimization substantially enhances Visual Language Processing accuracy. The comparative analysis validates superior positioning performance. The most accurate placement transpires at ground level. Increased power from Line of Sight diminishes positioning inaccuracy. The mean error in this instance is 0.59 cm. Multi-level modulation and Whale Optimization attain precision under 1 cm. These algorithms exhibit inferior precision compared to PSO.	Particle Swarm Optimization enhances localization precision, although it possesses certain restrictions. P&O provides swifter answers but diminished accuracy compared to PSO [91]. Particle Swarm Optimization may excessively utilize computational resources without meticulous calibration. In intricate scenarios, PSO enhances photovoltaic power points. Particle Swarm Optimization (PSO) surpasses conventional techniques under partial shading situations [91], [92].
Calibration and measurement of respiratory frequency	A representative pattern was examined for calibrating purposes. The peak points of each respiratory cycle were found. A measuring interval T was established. Gravitational acceleration of $9.8\ \text{m/s}^2$ facilitated signal scaling. A 16-bit MEMS sensor delivered exceptional precision. The total sensor scale was $R = 2^{16} = 16384$. This configuration guaranteed dependable respiratory assessments. An in-depth investigation of the respiratory cycle was conducted.	Sensor-based measurement of respiratory rate provides excellent precision. Performance fluctuates among many contexts and populations. Regulated conditions substantially enhance measurement accuracy. The positioning of sensors and their variability influence precision. External interferences may undermine measurement reliability. Regular recalibrations are necessary for consistent performance [93]. Machine learning enhances the reliability of respiratory monitoring. Adaptive algorithms improve system functionality and precision. Technological developments diminish variability and interferences. Enhanced methodologies guarantee consistent performance across varied environments [94].
Calibration of MEM sensors	The **SoC** calibration uses red and infrared light. Photodiodes detect reflected light for accurate measurement. An 18-bit ADC samples between 50 sps and 3200 sps. Calibration ensures precise oxygen saturation measurements. Results show normal variability and detect hypoxia onset. Oxygenated blood absorbs more infrared than red light. Deoxygenated blood absorbs more red than infrared light. This enables precise oxygen saturation determination. Effective in thin-skin areas with surface blood vessels. Ensures reliable oxygen level monitoring.	SoCs with PPG function effectively on places with thin skin. Fingertips and earlobes provide superior light penetration. Challenges encompass precision in low perfusion situations. Consistent skin contact continues to be a significant concern. Contactless techniques employ polarized imaging for enhancements. Advanced methodologies improve the precision of SpO_2 measurements [95].
The progression of the disease	The initial states are derived from the predictions in Table 7. Each state is binary with an initial chance of 100%. If $p(0) = [1\ \ 0\ \ 0\ \ 0\ \ 0]^T$, certainty is established. The processed data produced a heat map diagram. Figure 21 illustrates probability percentages as a function of time k. The heat map is contingent upon the input data A_{in}. The probability axis denotes state transitions and stability. Probabilities fluctuate markedly among iterations. Variability arises from distinct moments within data samples. Results are compatible with the evaluation input data.	Initial states are crucial in numerous applications. Delays in communication impact estimates in cyber-physical systems. In regulated settings, preliminary assessment is more straightforward. Latencies disrupt event sequencing and impede assessments. Robust methodologies mitigate the effects of network latency [96]. Probabilities fluctuate based on the duration of sampling. The absence of continuity impedes state advancement. Consistent input data uphold system stability [96].

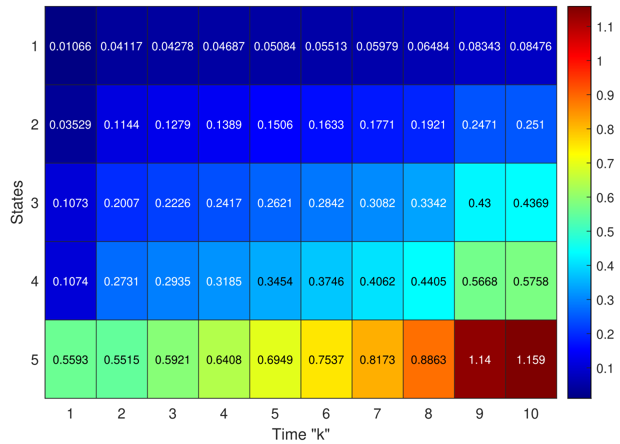

FIGURE 21. Heat map diagram showing the transition probabilities based on the input vector A_{in}.

7) Calibration of MEM sensors, and 8) The progression of the disease.

In addition, a comparative analysis is carried out that contrasts these results with previous studies.

While the analysis suggests that 40 iterations are optimal for convergence, this may vary depending on the specific application requirements and problem characteristics. Some applications may benefit from fewer iterations if computational resources are limited, while others may require more iterations to achieve higher accuracy. Efficient convergence with minimal iterations reduces computational load, making PSO suitable for resource-constrained applications [90].

Additionally, the use of adaptive PSO variants can further optimize convergence by dynamically adjusting parameters throughout the optimization process.

A. LIMITATIONS

The VLP programs were evaluated in the laboratory through simulations without being implemented in hospital settings.

We worked considering a minimum mobility of patients within hospital wards.

VII. CONCLUSION

This study proposed an optimized physiological monitoring system for COVID-19 patients by integrating VLC-based 3D localization with Markov Chain Analysis, providing a real-time solution for tracking vital physiological parameters. The results demonstrated that the proposed method successfully balances localization precision and computational efficiency, making it a viable approach for healthcare applications.

The performance of the VLC-based localization system was evaluated using three LED beacons and Particle Swarm Optimization (PSO). The PSO analysis showed that cognitive and social components ($c_1 = 1.9$, $c_2 = 2.1$) significantly enhanced positioning accuracy, while an optimal inertia weight ($w = 0.8$) ensured a balance between exploration and convergence. The best trade-off between accuracy and computational cost was observed with 700 to 1100 particles.

MEMS sensors were used to measure and calibrate cough frequency, respiratory rate, and oxygen saturation (SpO_2). The cough frequency peaked at 0.2 Hz, supporting its use for symptom tracking. The respiratory cycle was detected at a mean rate of 1.3 breaths per minute, validated through MEMS-based acceleration analysis. The pulse oximeter system successfully detected hypoxia events using infrared and red light absorption, highlighting its capability for early identification of respiratory distress.

A Markov Chain Model was developed to predict disease progression based on heart rate, temperature, cough frequency, respiratory rate, and (SpO_2) levels. The model identified four distinct patient states, ranging from mild to severe conditions. The probabilities of transitioning between states showed that mild cases remained stable, while worsening symptoms significantly increased the likelihood of reaching a critical state. A heat map representation confirmed the validity of state transitions, reinforcing the model's ability to forecast disease progression.

This study also emphasized the trade-off between localization accuracy and computational cost. Increasing the number of PSO particles improved positioning accuracy, but at the expense of higher execution time. Similarly, reducing the inertia weight beyond the optimal range degraded system performance, stressing the importance of fine-tuning parameters for real-time implementation in healthcare environments.

FUTURE WORK

Future work will focus on studying the interference caused by white-light transmission and developing adaptive algorithms for the dynamic adjustment of PSO parameters to further optimize system performance. In addition, efforts will be made to generalize the solution for its application in the detection of other pathogens, expanding its scope and utility.

As local processors increase in capacity, it will become possible to efficiently run programs such as **DeepSeek** [97] and **Llama 3** [98], open-source artificial intelligence language models recognized for their performance and accessibility. These open-source alternatives enable exploration and research in various artificial intelligence applications, providing advanced tools for natural language processing [99].

It is important to unravel the influence of different variables and preparedness to COVID-19 incidence in order to prepare cities for future pandemics [100].

REFERENCES

[1] D. H. Tarhuni Navarro and N. Sanz Merino, "La autoridad cultural de la ciencia en tiempos pandémicos y la postnormalidad cultural en México," *Arbor*, vol. 198, no. 806, p. a677, Dec. 2022, doi: 10.3989/arbor.2022.806007.

[2] M. Peiris, "Lessons of the COVID-19 pandemic," *Ceylon Med. J.*, vol. 68, no. SI1, pp. 7–8, Aug. 2023, doi: 10.4038/cmj.v68isi1.9736.

[3] H. O. Garcés, C. Durán, E. Espinosa, A. Jerez, F. Palominos, M. Hinojosa, and R. Carrasco, "Monitoring of thermal comfort and air quality for sustainable energy management inside hospitals based on online analytical processing and the Internet of Things," *Int. J. Environ. Res. Public Health*, vol. 19, no. 19, p. 12207, Sep. 2022, doi: 10.3390/ijerph191912207.

[4] M. Campillay-Campillay, A. Calle-Carrasco, P. Dubo, J. Moraga-Rodríguez, J. Coss-Mandiola, J. Vanegas-López, A. Rojas, and R. Carrasco, ''Accessibility in people with disabilities in primary healthcare centers: A dimension of the quality of care,'' *Int. J. Environ. Res. Public Health*, vol. 19, no. 19, p. 12439, Sep. 2022, doi: 10.3390/ijerph191912439.

[5] X. Alvial, A. Rojas, R. Carrasco, C. Durán, and C. Fernández-Campusano, ''Overuse of health care in the emergency services in Chile,'' *Int. J. Environ. Res. Public Health*, vol. 18, no. 6, p. 3082, Mar. 2021, doi: 10.3390/ijerph18063082.

[6] D. A. Candia, P. P. Játiva, C. Azurdia Meza, I. Sánchez, and M. Ijaz, ''Performance analysis of the particle swarm optimization algorithm in a VLC system for localization in hospital environments,'' *Appl. Sci.*, vol. 14, no. 6, p. 2514, Mar. 2024, doi: 10.3390/app14062514.

[7] J. Wichmann, ''Indoor positioning systems in hospitals: A scoping review,'' *Digit. HEALTH*, vol. 8, Jan. 2022, Art. no. 205520762210816, doi: 10.1177/20552076221081696.

[8] J. Coss-Mandiola, J. Vanegas-López, A. Rojas, R. Carrasco, P. Dubo, and M. Campillay-Campillay, ''Characterization of communes with quality accredited primary healthcare centers in Chile,'' *Int. J. Environ. Res. Public Health*, vol. 19, no. 15, p. 9189, Jul. 2022, doi: 10.3390/ijerph19159189.

[9] J. Coss-Mandiola, J. Vanegas-López, A. Rojas, P. Dubó, M. Campillay-Campillay, and R. Carrasco, ''Accreditation of quality in primary health care in Chile: Perception of the teams from accredited family healthcare centers,'' *Int. J. Environ. Res. Public Health*, vol. 20, no. 3, p. 2477, Jan. 2023, doi: 10.3390/ijerph20032477.

[10] J. Luo, L. Fan, and H. Li, ''Indoor positioning systems based on visible light communication: State of the art,'' *IEEE Commun. Surveys Tuts.*, vol. 19, no. 4, pp. 2871–2893, 4th Quart., 2017, doi: 10.1109/COMST.2017.2743228.

[11] H. Wang, J. Tian, S. Li, H. Zhao, F. Wu, and X. Li, ''Structure-conditioned adversarial learning for unsupervised domain adaptation,'' *Neurocomputing*, vol. 497, pp. 216–226, Aug. 2022, doi: 10.1016/j.neucom.2022.04.094.

[12] P. Zhu, S. Gong, X. Zhao, and X. Sun, ''A review: Machine learning in visible light wireless positioning system,'' in *Proc. 2nd Int. Conf. Netw. Syst. AI (INSAI)*. Shanghai, China, Oct. 2022, pp. 126–132, doi: 10.1109/INSAI56792.2022.00032.

[13] Z. Li, A. Yang, H. Lv, L. Feng, and W. Song, ''Fusion of visible light indoor positioning and inertial navigation based on particle filter,'' *IEEE Photon. J.*, vol. 9, no. 5, pp. 1–13, Oct. 2017, doi: 10.1109/JPHOT.2017.2733556.

[14] X. Wang and J. Shen, ''Machine learning and its applications in visible light communication based indoor positioning,'' in *Proc. Int. Conf. High Perform. Big Data Intell. Syst.*, May 2019, pp. 274–277, doi: 10.1109/HPBDIS.2019.8735490.

[15] W. Wang, J. Zhang, Q. Wang, and M. Zuniga, ''Leveraging smart lights for passive localization,'' in *Proc. IEEE 15th Int. Conf. Mobile Ad Hoc Sensor Syst. (MASS)*, Chengdu, China, Oct. 2018, pp. 272–280, doi: 10.1109/MASS.2018.00049.

[16] N. Faulkner, F. Alam, M. Legg, and S. Demidenko, ''Smart wall: Passive visible light positioning with ambient light only,'' in *Proc. IEEE Int. Instrum. Meas. Technol. Conf. (I2MTC)*, Auckland, New Zealand, May 2019, pp. 1–6, doi: 10.1109/I2MTC.2019.8826875.

[17] K. Majeed and S. Hranilovic, ''Passive indoor localization for visible light communication systems,'' in *Proc. IEEE Global Commun. Conf. (GLOBECOM)*, Dec. 2018, pp. 1–6, doi: 10.1109/GLOCOM.2018.8647875.

[18] D. Wang, D. Tan, and L. Liu, ''Particle swarm optimization algorithm: An overview,'' *Soft Comput.*, vol. 22, no. 2, pp. 387–408, Jan. 2018, doi: 10.1007/s00500-016-2474-6.

[19] C. Carreño, F. Seguel, P. Adasme, I. Soto, N. Krommenacker, P. Charpentier, and V. Bombardier, ''Comparison of metaheuristic optimization algorithms for RSS-based 3-D visible light positioning systems,'' in *Proc. South Amer. Colloq. Visible Light Commun. (SACVC)*, Santiago, Chile, Jun. 2020, pp. 1–6, doi: 10.1109/SACVLC50805.2020.9129861.

[20] Y. Cai, W. Guan, Y. Wu, C. Xie, Y. Chen, and L. Fang, ''Indoor high precision three-dimensional positioning system based on visible light communication using particle swarm optimization,'' *IEEE Photon. J.*, vol. 9, no. 6, pp. 1–20, Dec. 2017, doi: 10.1109/JPHOT.2017.2771828.

[21] F. Seguel, P. Palacios-Játiva, C. A. Azurdia-Meza, N. Krommenacker, P. Charpentier, and I. Soto, ''Underground mine positioning: A review,'' *IEEE Sensors J.*, vol. 22, no. 6, pp. 4755–4771, Mar. 2022, doi: 10.1109/JSEN.2021.3112547.

[22] Z. Pan, J. Carleton, S. Zeng, T. Lang, G. Chen, and A. Wang, ''Indoor tracking for smart hospital by a hybrid visible light positioning system,'' *J. Auto. Intell.*, vol. 6, no. 3, p. 576, Sep. 2023, doi: 10.32629/jai.v6i3.576.

[23] V. Rekkas, L. Iliadis, S. Sotiroudis, A. Boursianis, P. Sarigiannidis, D. Plets, W. Joseph, S. Wan, C. Christodoulou, G. Karagiannidis, and S. Goudos, ''Artificial intelligence in visible light positioning for indoor IoT: A methodological review,'' *IEEE Open J. Commun. Soc.*, vol. 4, pp. 2838–2869, 2023, doi: 10.1109/OJCOMS.2023.3327211.

[24] J. S. Sunny, C. P. K. Patro, K. Karnani, S. C. Pingle, F. Lin, M. Anekoji, L. D. Jones, S. Kesari, and S. Ashili, ''Anomaly detection framework for wearables data: A perspective review on data concepts, data analysis algorithms and prospects,'' *Sensors*, vol. 22, no. 3, p. 756, Jan. 2022, doi: 10.3390/s22030756.

[25] M. Sliti, M. Mrabet, M. Garai, and L. B. Ammar, ''A survey on machine learning algorithm applications in visible light communication systems,'' *Opt. Quantum Electron.*, vol. 56, no. 8, p. 1351, Jul. 2024, doi: 10.1007/s11082-024-06862-1.

[26] F. Wei, Y. Wu, S. Xu, and X. Wang, ''Accurate visible light positioning technique using extreme learning machine and meta-heuristic algorithm,'' *Opt. Commun.*, vol. 532, Apr. 2023, Art. no. 129245, doi: 10.1016/j.optcom.2022.129245.

[27] S.-H. Oh and J.-G. Kim, ''AI-based positioning with input parameter optimization in indoor VLC environments,'' *Sensors*, vol. 22, no. 21, p. 8125, Oct. 2022, doi: 10.3390/s22218125.

[28] M. Morales-Céspedes, J. Pérez-Aracil, A. García-Armada, and S. Salcedo-Sanz, ''Learning for visible light communications: Potential scenarios and applications,'' *IEEE Consum. Electron. Mag.*, vol. 9, no. 1, pp. 1–14, Jan. 2025, doi: 10.1109/MCE.2025.3525584.

[29] X. Sun, Y. Zhuang, J. Huai, L. Hua, D. Chen, Y. Li, Y. Cao, and R. Chen, ''RSS-based visible light positioning using nonlinear optimization,'' *IEEE Internet Things J.*, vol. 9, no. 15, pp. 14137–14150, Aug. 2022, doi: 10.1109/JIOT.2022.3156616.

[30] K. Vijayakumari and K. Anusudha, ''Survey of hybrid deep learning autoencoders for enhanced visible light communication systems,'' *Proc. Comput. Sci.*, vol. 252, pp. 100–107, Feb. 2025, doi: 10.1016/j.procs.2024.12.011.

[31] W. M. Salama, M. H. Aly, and E. S. Amer, ''VLC localization: Deep learning models by Kalman filter algorithm combined with RSS,'' *Opt. Quantum Electron.*, vol. 54, no. 9, p. 584, Sep. 2022, doi: 10.1007/s11082-022-03985-1.

[32] M. Razzaq and I. Abdullah, ''Accuracy enhancement in indoor positioning system based on visible light communication,'' *Periodicals Eng. Natural Sci. (PEN)*, vol. 10, no. 3, pp. 300–310, Jun. 2022, doi: 10.21533/pen.v10i3.3030.

[33] X. Ren, Z. Zhao, L. Sun, X. Li, Z. Dong, and Y. Zhang, ''Based on reflected light depolarization characteristics optimization method for improving indoor visible light positioning accuracy,'' *Opt. Eng.*, vol. 61, no. 5, May 2022, Art. no. 056101, doi: 10.1117/1.oe.61.5.056101.

[34] M. R. Abdali and I. A. Murdas, ''Modified maximum liklehood approach in indoor positioning system based on VLC technology,'' in *Proc. 5th Int. Conf. Eng. Technol. its Appl. (IICETA)*, May 2022, pp. 390–397, doi: 10.1109/IICETA54559.2022.9888526.

[35] R. A. Martínez-Ciro, F. E. López-Giraldo, J. M. Luna-Rivera, and A. M. Ramírez-Aguilera, ''An indoor visible light positioning system for multi-cell networks,'' *Photonics*, vol. 9, no. 3, p. 146, Mar. 2022, doi: 10.3390/photonics9030146.

[36] X. Meng, C. Jia, C. Cai, F. He, and Q. Wang, ''Indoor high-precision 3D positioning system based on visible-light communication using improved whale optimization algorithm,'' *Photonics*, vol. 9, no. 2, p. 93, Feb. 2022, doi: 10.3390/photonics9020093.

[37] I. Cappelli, F. Carli, A. Fort, M. Intravaia, F. Micheletti, G. Peruzzi, and V. Vignoli, ''Enhanced visible light localization based on machine learning and optimized fingerprinting in wireless sensor networks,'' *IEEE Trans. Instrum. Meas.*, vol. 72, pp. 1–10, 2023, doi: 10.1109/TIM.2023.3240220.

[38] J. Zhu, M. Lin, J. Xing, B. Chen, Z. Gu, Z. Zhang, and Y. Xu, ''Tilted-angle insensitive received signal strength in visible light positioning systems using a deep neural network trained by synthetic data,'' *AIP Adv.*, vol. 13, no. 6, Jun. 2023, Art. no. 065204, doi: 10.1063/5.0147861.

[39] H. C. Ates, A. K. Yetisen, F. Güder, and C. Dincer, ''Wearable devices for the detection of COVID-19,'' *Nature Electron.*, vol. 4, no. 1, pp. 13–14, Jan. 2021, doi: 10.1038/s41928-020-00533-1.

[40] M. Baldinger, A. Heinrich, T. Adams, E. Martens, M. Dommasch, A. Müller, A. Siegmann, and G. Schmidt, "TELECOVID: Remote vital signs monitoring of COVID-19 risk patients in home isolation with an in-ear wearable," *IEEE Pervasive Comput.*, vol. 20, no. 2, pp. 58–62, Apr. 2021, doi: 10.1109/MPRV.2021.3066825.
[41] T. Mishra et al., "Pre-symptomatic detection of COVID-19 from smartwatch data," *Nature Biomed. Eng.*, vol. 4, no. 12, pp. 1208–1220, Nov. 2020, doi: 10.1038/s41551-020-00640-6.
[42] J. R. Donsimoni, R. Glawion, B. Plachter, and K. Wälde, "Projecting the spread of COVID-19 for Germany," *German Econ. Rev.*, vol. 21, no. 2, pp. 181–216, Jun. 2020, doi: 10.1515/ger-2020-0031.
[43] K. Larimer, S. Wegerich, J. Splan, D. Chestek, H. Prendergast, and T. V. Hoek, "Personalized analytics and a wearable biosensor platform for early detection of COVID-19 decompensation (DeCODe): Protocol for the development of the COVID-19 decompensation index," *JMIR Res. Protocols*, vol. 10, no. 5, May 2021, Art. no. e27271, doi: 10.2196/27271.
[44] C. Cislo, C. Clingan, K. Gilley, M. Rozwadowski, I. Gainsburg, C. Bradley, J. Barabas, E. Sandford, M. Olesnavich, J. Tyler, C. Mayer, M. DeMoss, C. Flora, D. B. Forger, J. L. Cunningham, M. Tewari, and S. W. Choi, "Monitoring beliefs and physiological measures using wearable sensors and smartphone technology among students at risk of COVID-19: Protocol for a mHealth study," *JMIR Res. Protocols*, vol. 10, no. 6, Jun. 2021, Art. no. e29561, doi: 10.2196/29561.
[45] F. Ullah, H. U. Haq, J. Khan, A. A. Safeer, U. Asif, and S. Lee, "Wearable IoTs and geo-fencing based framework for COVID-19 remote patient health monitoring and quarantine management to control the pandemic," *Electronics*, vol. 10, no. 16, p. 2035, Aug. 2021, doi: 10.3390/electronics10162035.
[46] H. Jeong, J. A. Rogers, and S. Xu, "Continuous on-body sensing for the COVID-19 pandemic: Gaps and opportunities," *Sci. Adv.*, vol. 6, no. 36, pp. 1–5, Sep. 2020, doi: 10.1126/sciadv.abd4794.
[47] L. Lonini, N. Shawen, O. Botonis, M. Fanton, C. Jayaraman, C. K. Mummidisetty, S. Y. Shin, C. Rushin, S. Jenz, S. Xu, J. A. Rogers, and A. Jayaraman, "Rapid screening of physiological changes associated with COVID-19 using soft-wearables and structured activities: A pilot study," *IEEE J. Transl. Eng. Health Med.*, vol. 9, pp. 1–11, 2021, doi: 10.1109/JTEHM.2021.3058841.
[48] F. D. A. Guidali, L. Zanatta, A. C. Pilatti, F. N. C. Lopes, F. C. S. Ferreira, and V. V. Dos Santos, "Factores de riesgo individuales asociados con la infección por COVID-19," *Contribuciones Las Ciencias Sociales*, vol. 16, no. 10, pp. 20498–20515, Oct. 2023, doi: 10.55905/revconv.16n.10-110.
[49] E. O. Páez, J. E. C. Pozo, M. Á. A. F. de Bobadilla, M. V. G. Gómez, J. L. S. Pérez, B. J. Moreno, B. S. Pérez, and S. M. Díaz, "Es posible ofrecer un algoritmo de decisión clínica en la enfermedad COVID-19 en Atención primaria?" *Revista Pediatría Atención Primaria*, vol. 22, no. 5, pp. 423–433, May 2020.
[50] A. Natarajan, H.-W. Su, and C. Heneghan, "Assessment of physiological signs associated with COVID-19 measured using wearable devices," *Npj Digit. Med.*, vol. 3, no. 1, p. 156, Nov. 2020, doi: 10.1038/s41746-020-00363-7.
[51] R. P. Hirten et al., "Use of physiological data from a wearable device to identify SARS-CoV-2 infection and symptoms and predict COVID-19 diagnosis: Observational study," *J. Med. Internet Res.*, vol. 23, no. 2, pp. 1–14, Feb. 2021, doi: 10.2196/26107.
[52] J. Phipps, B. Passage, K. Sel, J. Martinez, M. Saadat, T. Koker, N. Damaso, S. Davis, J. Palmer, K. Claypool, C. Kiley, R. I. Pettigrew, and R. Jafari, "Early adverse physiological event detection using commercial wearables: Challenges and opportunities," *npj Digit. Med.*, vol. 7, no. 1, p. 136, May 2024, doi: 10.1038/s41746-024-01129-1.
[53] A. Sbrollini, I. Marcantoni, T. Lunghi, M. Morettini, and L. Burattini, "Cardiorespiratory DB: Collection of cardiorespiratory data acquired during normal breathing, deep breathing and breath holding," *Data Brief*, vol. 54, Jun. 2024, Art. no. 110406, doi: 10.1016/j.dib.2024.110406.
[54] S. Dimitrov and H. Haas, "Optical wireless communication," in *Principles of LED Light Communications: Towards Networked Li-Fi*. Cambridge, U.K.: Cambridge Univ. Press, 2024, ch. 2, pp. 12–56.
[55] L. He, L. Shi, X. Li, and M. Sun, "Supermarket commodity guide system based on indoor visible light positioning," in *Proc. 5th World Symp. Commun. Eng. (WSCE)*, Nagoya, Japan, Sep. 2022, pp. 33–37, doi: 10.1109/WSCE56210.2022.9916022.
[56] P. P. Játiva, C. A. Azurdia-Meza, I. Sánchez, F. Seguel, D. Zabala-Blanco, A. D. Firoozabadi, C. A. Gutiérrez, and I. Soto, "A VLC channel model for underground mining environments with scattering and shadowing," *IEEE Access*, vol. 8, pp. 185445–185464, 2020, doi: 10.1109/ACCESS.2020.3030615.
[57] W. Guan, Y. Wu, S. Wen, H. Chen, C. Yang, Y. Chen, and Z. Zhang, "A novel three-dimensional indoor positioning algorithm design based on visible light communication," *Opt. Commun.*, vol. 392, pp. 282–293, Jun. 2017, doi: 10.1016/j.optcom.2017.02.015.
[58] S. Yahia, Y. Meraihi, A. Ramdane-Cherif, A. B. Gabis, D. Acheli, and H. Guan, "A survey of channel modeling techniques for visible light communications," *J. Netw. Comput. Appl.*, vol. 194, Nov. 2021, Art. no. 103206, doi: 10.1016/j.jnca.2021.103206.
[59] S. Bastiaens, M. Alijani, W. Joseph, and D. Plets, "Visible light positioning as a next-generation indoor positioning technology: A tutorial," *IEEE Commun. Surveys Tuts.*, vol. 26, no. 4, pp. 2867–2913, 4th Quart., 2024, doi: 10.1109/COMST.2024.3372153.
[60] Z. Zhu, Y. Yang, M. Chen, C. Guo, J. Cheng, and S. Cui, "A survey on indoor visible light positioning systems: Fundamentals, applications, and challenges," 2024, *arXiv:2401.13893*.
[61] I. Soto, R. Zamorano-Illanes, R. Becerra, P. Palacios Játiva, C. A. Azurdia-Meza, W. Alavia, V. García, M. Ijaz, and D. Zabala-Blanco, "A new COVID-19 detection method based on CSK/QAM visible light communication and machine learning," *Sensors*, vol. 23, no. 3, p. 1533, Jan. 2023, doi: 10.3390/s23031533.
[62] C. Lee and W. J. Choi, "Overview of COVID-19 inflammatory pathogenesis from the therapeutic perspective," *Arch. Pharmacal Res.*, vol. 44, no. 1, pp. 99–116, Jan. 2021, doi: 10.1007/s12272-020-01301-7.
[63] C. M. A. Van Ravenswaaij-Arts, L. A. A. Kollee, J. C. W. Hopman, G. B. Stoelinga, and H. P. van Geijn, "Heart rate variability," *Ann. Internal Med.*, vol. 118, no. 6, pp. 436–447, Mar. 1993, doi: 10.7326/0003-4819-118-6-199303150-00008.
[64] E. Viera, H. Kaschel, and C. Valencia, "ECG processing algorithm in the QRS complex," in *Proc. IEEE Int. Conf. Automat. 24th Congr. Chilean Assoc. Autom. Control (ICA-ACCA)*, Mar. 2021, pp. 1–7, doi: 10.1109/ICAACCA51523.2021.9465280.
[65] E. Viera, H. Kaschel, and C. Valencia, "Heart rate variability control using a biofeedback and wearable system," *Sensors*, vol. 22, no. 19, p. 7153, Sep. 2022, doi: 10.3390/s22197153.
[66] A. S. Leon, B. A. Franklin, F. Costa, G. J. Balady, K. A. Berra, K. J. Stewart, P. D. Thompson, M. A. Williams, and M. S. Lauer, "Cardiac rehabilitation and secondary prevention of coronary heart disease," *Circulation*, vol. 111, no. 3, pp. 369–376, Jan. 2005, doi: 10.1161/01.cir.0000151788.08740.5c.
[67] F. Piccinini, G. Martinelli, and A. Carbonaro, "Reliability of body temperature measurements obtained with contactless infrared point thermometers commonly used during the COVID-19 pandemic," *Sensors*, vol. 21, no. 11, p. 3794, May 2021, doi: 10.3390/s21113794.
[68] K. Soltesz, *Dynamical Modeling of Physiology*. Lund, Sweden: Lund University, Mar. 2024, doi: 10.37852/oblu.258.
[69] L. F. Aragón-Vargas, "Limitaciones de la lectura de la temperatura temporal (en la frente) como método de tamizaje para el COVID-19," *Pensar en Movimiento: Revista de Ciencias del Ejercicio y la Salud*, vol. 18, no. 1, Jun. 2020, Art. no. e42291, doi: 10.15517/pensarmov.v18i1.42291.
[70] A. C. Villa-Parra, I. Criollo, C. Valadão, L. Silva, Y. Coelho, L. Lampier, L. Rangel, G. Sharma, D. Delisle-Rodríguez, J. Calle-Siguencia, F. Urgiles-Ortiz, C. Díaz, E. Caldeira, S. Krishnan, and T. Bastos-Filho, "Towards multimodal equipment to help in the diagnosis of COVID-19 using machine learning algorithms," *Sensors*, vol. 22, no. 12, p. 4341, Jun. 2022, doi: 10.3390/s22124341.
[71] A. Abdel-Ghani, A. Abdalla, Z. Abughazzah, M. Akhund, K. Abualsaud, and E. Yaacoub, "Wearable bracelet and machine learning for remote diagnosis and pandemic infection detection," *Discover Appl. Sci.*, vol. 6, no. 9, p. 451, Aug. 2024, doi: 10.1007/s42452-024-06156-x.
[72] P. García-Vicente, A. Rodríguez-Valiente, C. G. Gil, R. M. Altemir, F. Martínez-Pérez, L. F. López-Pajaro, and J. R. García-Berrocal, "Chronic cough in post-COVID syndrome: Laryngeal electromyography findings in vagus nerve neuropathy," *PLoS ONE*, vol. 18, no. 3, Mar. 2023, Art. no. e0283758, doi: 10.1371/journal.pone.0283758.
[73] S. Alsuwaidan, Z. A. Memish, F. Alaklobi, K. Khan, and H. N. Alajami, "The utilization of hydroxychloroquine to reduce the main signs and symptoms of COVID-19 patients, a cross-sectional study," *Ann. Med. Surg.*, vol. 70, Oct. 2021, Art. no. 102867, doi: 10.1016/j.amsu.2021.102867.
[74] Y. Singh, C. B. Pandey, S. Pandey, N. Chandola, and D. Agarwal, "Comprehensive cardiac monitoring and early intervention in a patient with hypertension using smartphone-based portable electrocardiogram," *J. Indian College Cardiol.*, vol. 15, pp. 27–31, Feb. 2025, doi: 10.4103/jicc.jicc_54_24.

[75] V. E. Papageorgiou, "Novel stochastic descriptors of a Markovian SIRD model for the assessment of the severity behind epidemic outbreaks," *J. Franklin Inst.*, vol. 361, no. 12, Aug. 2024, Art. no. 107022, doi: 10.1016/j.jfranklin.2024.107022.
[76] I. M. Attia, "Novel approach of multistate Markov chains to evaluate progression in the expanded model of non-alcoholic fatty liver disease," *Frontiers Appl. Math. Statist.*, vol. 7, Feb. 2022, Art. no. 766085, doi: 10.3389/fams.2021.766085.
[77] Z. Wang, Z. Liang, X. Li, and H. Li, "Indoor visible light positioning based on improved particle swarm optimization method with min-max algorithm," *IEEE Access*, vol. 10, pp. 130068–130077, 2022, doi: 10.1109/ACCESS.2022.3228543.
[78] A. Rezaee Jordehi and J. Jasni, "Parameter selection in particle swarm optimisation: A survey," *J. Experim. Theor. Artif. Intell.*, vol. 25, no. 4, pp. 527–542, Dec. 2013, doi: 10.1080/0952813x.2013.782348.
[79] Z. Liu and T. Nishi, "Strategy dynamics particle swarm optimizer," *Inf. Sci.*, vol. 582, pp. 665–703, Jan. 2022, doi: 10.1016/j.ins.2021.10.028.
[80] M. E. H. Pedersen and A. J. Chipperfield, "Simplifying particle swarm optimization," *Appl. Soft Comput.*, vol. 10, no. 2, pp. 618–628, Mar. 2010, doi: 10.1016/j.asoc.2009.08.029.
[81] D. Peng, G. Tan, K. Fang, L. Chen, P. K. Agyeman, and Y. Zhang, "Multiobjective optimization of an off-road vehicle suspension parameter through a genetic algorithm based on the particle swarm optimization," *Math. Problems Eng.*, vol. 2021, pp. 1–14, Jan. 2021.
[82] Z. Li-ping, Y. Huan-jun, and H. Shang-Xu, "Optimal choice of parameters for particle swarm optimization," *J. Zhejiang Univ.-Sci. A*, vol. 6, no. 6, pp. 528–534, Jun. 2005, doi: 10.1631/jzus.2005.a0528.
[83] T. M. Shami, A. A. El-Saleh, M. Alswaitti, Q. Al-Tashi, M. A. Summakieh, and S. Mirjalili, "Particle swarm optimization: A comprehensive survey," *IEEE Access*, vol. 10, pp. 10031–10061, 2022, doi: 10.1109/ACCESS.2022.3142859.
[84] G. Ji, K. Zhang, B. Zhang, and D. Yang, "Analysis of search anda rescue positioning accuracy based on improved particle swarm optimization algorithm," *Proc. SPIE*, vol. 12988, p. 82, Feb. 2024, doi: 10.1117/12.3024850.
[85] X. Wang, X. Wang, C. Gao, and J. Wu, "Positioning accuracy optimization of DSO-SLAM and its use for the localization of unmanned vehicle," in *Proc. Int. Conf. Comput. Commun. Artif. Intell. (CCAI)*, May 2021, pp. 155–160, doi: 10.1109/ccai50917.2021.9447457.
[86] S. Sivakumar, R. Venkatesan, and M. Karthiga, "Evolutionary approaches for minimising error in localisation of wireless sensor networks," *Int. J. Sensor Netw.*, vol. 17, no. 1, pp. 17–26, 2015, doi: 10.1504/ijsnet.2015.067587.
[87] M. Sabir, A. Ahmad, A. Ahmed, S. Siddique, and U. A. Hashmi, "A modified inertia weight control of particle swarm optimization for optimal reactive power dispatch problem," in *Proc. Int. Conf. Emerg. Power Technol. (ICEPT)*, Apr. 2021, pp. 1–6, doi: 10.1109/ICEPT51706.2021.9435588.
[88] K. R. Harrison, B. M. Ombuki-Berman, and A. P. Engelbrecht, "An analysis of control parameter importance in the particle swarm optimization algorithm," in *Proc. Int. Conf. Swarm Intell.*, vol. 11655. Cham, Switzerland: Springer, 2019, pp. 93–105.
[89] W. Yang, X. Zhou, and Y. Luo, "Simultaneously optimizing inertia weight and acceleration coefficients via introducing new functions into PSO algorithm," *J. Phys., Conf. Ser.*, vol. 1754, no. 1, Feb. 2021, Art. no. 012195, doi: 10.1088/1742-6596/1754/1/012195.
[90] Y. Romasevych, V. Loveikin, and A. Loveikin, "Investigation of an influence of a ratio, swarm size-iterations number on particle swarm optimization performance," in *Proc. IEEE 3rd KhPI Week Adv. Technol. (KhPIWeek)*. Kharkiv, Ukraine, Oct. 2022, pp. 1–4, doi: 10.1109/KHPIWEEK57572.2022.9916498.
[91] M. S. Endiz, "Performance analysis of P&O and PSO MPPT algorithms for PV systems under partial shading," *Konya J. Eng. Sci.*, vol. 12, no. 1, pp. 84–99, Dec. 2023, doi: 10.36306/konjes.1359177.
[92] M. A. Azad, M. Tariq, A. Sarwar, I. Sajid, S. Ahmad, F. I. Bakhsh, and A. E. Sayed, "A particle swarm optimization-adaptive weighted delay velocity-based fast-converging maximum power point tracking algorithm for solar PV generation system," *Sustainability*, vol. 15, no. 21, p. 15335, Oct. 2023, doi: 10.3390/su152115335.
[93] M. Sabz, J. MacLean, A. R. Martin, and H. Rouhani, "Characterization of wearable respiratory sensors for breathing parameter measurements," *IEEE Sensors J.*, vol. 24, no. 20, pp. 32283–32290, Oct. 2024, doi: 10.1109/JSEN.2024.3448539.
[94] D. E. Chickrin, A. A. Egorchev, D. M. Pashin, and N. A. Sarambaev, "Development of a system for determining the frequency of surface respiration according to smartphone biometric sensors," *Izvestiya SFedU. Eng. Sci.*, vol. 2023, no. 4, pp. 35–42, 2023, doi: 10.18522/2311-3103-2023-4-35-42.
[95] D. Mishra, N. Priyadarshini, S. Chakraborty, and M. Sarkar, "Blood oxygen saturation measurement using polarization-dependent optical sectioning," *IEEE Sensors J.*, vol. 17, no. 12, pp. 3900–3908, Jun. 2017, doi: 10.1109/JSEN.2017.2698520.
[96] Y. Yao, Y. Tong, and H. Lan, "Initial-state estimation of multi-channel networked discrete event systems," *IEEE Control Syst. Lett.*, vol. 4, no. 4, pp. 1024–1029, Oct. 2020, doi: 10.1109/LCSYS.2020.2998610.
[97] Q. Zhu et al., "DeepSeek-Coder-v2: Breaking the barrier of closed-source models in code intelligence," 2024, *arXiv:2406.11931*.
[98] B. Rozière et al., "Code llama: Open foundation models for code," 2023, *arXiv:2308.12950*.
[99] F. Reveco-Toledo, I. Soto, and V. Garcia, "Automated biological analysis system: Integration of chatbots and edge computing," in *Proc. IEEE Int. Conf. Autom., 24th Congr. Chilean Assoc. Autom. Control (ICA-ACCA)*, Chile, Oct. 2024, pp. 1–6, doi: 10.1109/ICA-ACCA62622.2024.10766799.
[100] K. Kuschel, R. Carrasco, B. J. Idrovo-Aguirre, C. Duran, and J. E. Contreras-Reyes, "Preparing cities for future pandemics: Unraveling the influence of urban and housing variables on COVID-19 incidence in Santiago de Chile," *Healthcare*, vol. 11, no. 16, p. 2259, Aug. 2023, doi: 10.3390/HEALTHCARE11162259.
[101] R. S. Abdulsadig and E. Rodriguez-Villegas, "Sleep posture monitoring using a single neck-situated accelerometer: A proof-of-concept," *IEEE Access*, vol. 11, pp. 17693–17706, 2023.
[102] V. H. de Souza et al., "Vital signs and laboratory tests dataset for COVID-19," PhysioNet, Tech. Rep., 2022, doi: 10.13026/7az3-hc80.
[103] Hospital Sírio-Libanes. (2020). *COVID-19: Clinical Data to Assess Diagnosis*. [Online]. Available: https://www.kaggle.com/datasets/S?rio-Libanes/covid19
[104] A. L. Goldberger, L. A. N. Amaral, L. Glass, J. M. Hausdorff, P. C. Ivanov, R. G. Mark, J. E. Mietus, G. B. Moody, C.-K. Peng, and H. E. Stanley. (2016). *MIMIC-III Waveform Database*. PhysioNet. [Online]. Available: https://physionet.org/content/mimic3wdb/1.0/

EDUARDO VIERA RIQUELME received the master's degree in telecommunications and the Ph.D. degree in engineering sciences, with specialization in automatic from the Department of Electrical Engineering, Universidad de Santiago de Chile. He is a part time Professor with the Universidad de Santiago de Chile. His research lines are focused on the automatic control application, wireless sensor networks, and IA applications.

DIEGO ALONSO CANDIA received the degree in civil engineering in informatics and telecommunications from Diego Portales University, Chile. He is currently a Software Engineer with the banking sector. He is also involved in the FONDECYT Project Advances in Visible Light Communications Applied to Industry Environments, conducting research on the application of visible light communication (VLC) for indoor localization. His professional interests include software development, telecommunications, and emerging technologies in industrial environments.

ISMAEL SOTO (Member, IEEE) was born in Punta Arenas, Chile. He received the degree in engineering from the University of Santiago of Chile, in 1982, the Master of Engineering degree from University Federico Santa Maria, in 1990, and the Ph.D. degree from the University of Staffordshire, U.K., in 1997. He has taught with the Department of Computer Science, the Department of Industrial Engineering, and the Department of Electrical Engineering, University of Santiago of Chile, where he is currently an Associate Professor of telecommunications and signal processing with the Electrical Engineering Department. He has been the National Director and a member of the International Speech Communication Association. He has participated in several national and international research projects on radio and visible light communication technology. He registers patents in several countries. His research interests include safety, DSP, visible light communications, and big data. He received the Innovation Award from the Association of Electrical Engineers (AIE). He has been an ITC of CSNDSP and the Chairman of the Organizing Committee of SACVLC. He has been a Reviewer for multiple journals, such as *Optimization*, *IET Communications*, and *Optik*.

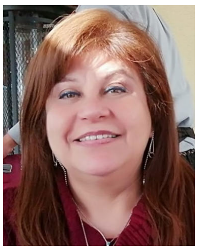

CAROLINA LAGOS received the master's degree in business management from UTFSM, the M.B.A. degree from the UP de Cataluna, and the Ph.D. degree in administration sciences from USACH. She has experience in higher education and research in areas, such as efficiency energy, technological management, organizational behavior, and mining. She has extensive experience advising both national and international companies. She is a Specialist in technological innovation. She is a former President of ACCA and Chilean Automatic Control Association.

PABLO PALACIOS JÁTIVA (Member, IEEE) received the B.S. degree in electronics and telecommunications engineering from the Escuela Superior Politécnica del Litoral (ESPOL), Guayaquil, Ecuador, in 2013, and the master's degree in communications network engineering and the Ph.D. degree in electrical engineering from the University of Chile, Santiago, Chile, in 2017 and 2023, respectively. He is currently a Professor with Universidad Diego Portales, Santiago. His current research interests include modeling, design, and performance analysis of optical wireless communication; and RF communication systems. He has served as a technical program committee (TPC) member and a reviewer for multiple conferences. He was a reviewer of journals, such as IEEE Access IEEE Internet of Things Journal, and *IEEE Communications Magazine*.

RAÚL CARRASCO received the Diploma degree in instrumentation and industrial control, the master's degree in industrial engineering, and the Ph.D. degree in engineering sciences with a focus on automatic. He was a Commercial Engineer in business administration. He was a Public Accountant and an Auditor with the Universidad de Santiago de Chile. He was a Professor with the Universidad de Santiago de Chile, the Universidad de Las Américas, and Andrés Bello University. He is currently a Professor-Investigator with Metropolitan Technological University. His research interests include forecasting, chaos, decision making, health, and sustainability.

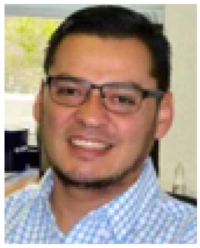

CESAR AZURDIA MEZA (Member, IEEE) received the B.Sc. degree in electronics engineering from the Universidad del Valle de Guatemala, Guatemala, in 2005, the M.Sc. degree in electrical engineering from Linnaeus University, Sweden, in 2009, and the Ph.D. degree in electronics and radio engineering from Kyung Hee University, Republic of Korea, in 2013. He joined the Department of Electrical Engineering, University of Chile, as an Assistant Professor, in August 2013. Since August 2021, he has been an Associate Professor with the University of Chile. His research interests include Nyquist's ISI criterion, OFDM-based systems, VLC systems, vehicular communications, and 5G and beyond enabling technologies. He is an IEEE Communications Society Member and a member of the IEICE Communications Society. He was a co-recipient of the 2019 IEEE LATINCOM Best Paper Award and the 2016 IEEE CONESCAPAN Best Paper Award. He was a supervisor of the awarded Ph.D. Thesis with the 2022 Abertis Award for Research in Road Safety (Ex-Aequo) at the national and international level.

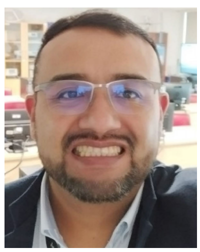

IVÁN SÁNCHEZ received the Engineering degree from the National Polytechnic School of Ecuador, in 2006, and the M.Eng. degree from the Central University of Ecuador, in 2015. He is currently pursuing the Ph.D. degree with the University of Malaga, Spain. He is also a Professor with the University of the Americas, Ecuador. His research interests include digital communications, electronic circuits, and electromagnetic theory.